Summer 8-8-2020

Multiphysics Computational Model of Fluid Flow and Mass Transport in Aneurysm

Tanja Cupac

MULTIPHYSICS COMPUTATIONAL MODEL OF FLUID FLOW AND MASS TRANSPORT IN ANEURYSM

A Thesis

Submitted to the John G. Rangos Sr. School of Health Sciences

Duquesne University

In partial fulfillment of the requirements for

the degree of Master of Science

By

Tanja Cupac

August 2020

MULTIPHYSICS COMPUTATIONAL MODEL OF FLUID FLOW AND MASS TRANSPORT IN ANEURYSM

By

Tanja Cupac

Approved June 25, 2020

_____ Rana Zakerzadeh, Ph.D. Assistant Professor of Engineering Committee Chair	_____ Richard Simpson, Ph.D. Associate Professor of Occupational Therapy Committee Member
_____ Melikhan Tanyeri, Ph,D. Assistant Professor of Engineering Committee Member	_____ Fevzi Akinci, Ph.D. Dean, John G. Rangos, Sr. School of Health Sciences Professor of Health Administration

_____
John Viator, Ph.D.
Chair, Department of Engineering
Professor of Biomedical Engineering

ABSTRACT

MULTIPHYSICS COMPUTATIONAL MODEL OF FLUID FLOW AND MASS TRANSPORT IN ANEURYSM

By

Tanja Cupac

August 2020

Dissertation supervised by Dr. Rana Zakerzadeh

The abdominal aortic aneurysm is progressive, asymptomatic, and can eventually lead to rupture which is a catastrophic event leading to massive internal bleeding and possibly death. AAA cases have been characterized by the development of an intraluminal thrombus (ILT). The ILT correlates with the progression of hypoxia in the arterial wall. The extent that ILT presence reduces oxygen flux to the wall has not been quantified and there is rather a poor understanding of key parameters that can affect thrombus-mediated oxygen transport in AAA. The purpose of this study is to address this gap and to assess the effects of different AAA geometric and physical features on the oxygen flow. We develop a modeling approach to investigate the association of ILT in AAA with local hypoxia. A sensitivity study is also performed to project oxygen fluctuations dependent on different model parameters including oxygen diffusivity, AAA

geometric features, and the effect of the vasa vasorum. Results confirm that the presence of an ILT reduces oxygen flux to the wall. Highly sensitive parameters such as the effect of the vasa vasorum and wall diffusivity are identified.

ACKNOWLEDGEMENT

I would first like to express my deepest gratitude to my thesis advisor Dr. Rana Zakerzadeh. She has truly been a wonderful mentor. I would like to thank her for her guidance, patience and knowledge in completing this project. The fashion in which she goes about her work is something I aspire toward in my future endeavors. I would also like to thank the committee members for reviewing my work. Finally, I would like to thank my family for their unwavering support.

TABLE OF CONTENTS

LIST OF FIGURES

Page

Chapter 1 – Introduction

The Abdominal Aortic Aneurysm (AAA) is the progressive focal dilation of diseased tissue in the infrarenal aorta. AAA mostly affects men between the ages 65-85 and is very common with more than 3 million cases in the United States per year, making an untreated AAA the 13th most common cause of death in the United States [1, 2]. Of the males within this age range, 1-3% will die as a result of aneurysmal rupture [3]. Clinical diagnostics utilize metrics derived from imaging modalities such as the MRI and CT to warrant emergency repair on aneurysms ranging from 5.0 and 5.5 cm in bulge diameter. However, studies show there is large variability between bulge diameter and risk of rupture. The issue remains in finding a more accurate way to predict rupture and avoid invasive surgery. The large variability between patients may be due to the presence of an intraluminal thrombus (ILT). About 80% of AAA cases will be characterized by the development of an ILT [4]. The beginning stages of ILT formation are characterized by aggregation of activated platelets and the buildup of enterocytes and leukocytes in a fibrin mesh [5]. The ILT is an isotropic, heterogenous, solid-like material that significantly changes shear wall stress and biomolecule transport [6]. Controversy surrounds the role of the ILT in aneurysmal pathogenesis. On one hand, the ILT is believed to enact as a "mechanically protective" layer due to its incompressible properties. In contrast, studies show thick ILT geometries result in poor diffusivity and active fibrin degradation within the ILT [7]. Slowed blood flow in the aneurysmal bulge triggers the body's immune system causing coagulation and inflammatory responses resulting in localized hypoxia of the luminal surface within the AAA [7]. External vessels undergo adventitial angiogenesis to provide supplemental oxygen to combat the limited diffusion of the ILT [8]. However, the wall is still depleted of necessary oxygen, degraded and weakened, ultimately leading to potential rupture. The extent

that ILT presence reduces oxygen flux to the arterial wall has not been quantified and there is rather a poor understanding of key parameters that can affect thrombus-mediated mass transport in AAA.

Despite supporting experimental studies utilizing uniaxial tensile measurements to characterize wall-strength variability hypothesized to be linked to ILT-induced hypoxia, there is little research on mass-transport of biomolecules within the AAA containing an ILT [5]. Comprehensive computational models with key biomechanical parameters are lacking and no previous studies have considered oxygen distribution from both a geometric and physiological stand-point. Thus, biochemical and biomechanical computational models will improve risk of rupture analysis.

Previous models range in complexity and geometry. Certain studies have focused either on the mechanics or the hemodynamics of the AAA in the absence of a thrombus. In cases where the ILT is modeled, coupled fluid dynamics equations with mass-transport through the thrombus and arterial-wall are neglected [5, 9]. In particular, Vorp considers an idealized, axisymmetric geometry of an AAA with an ILT that uses diffusion equations to model oxygen flux in the thrombus layer with a representative interior partial pressure of luminal oxygen concentration [5]. The study was successful in modeling the effect of ILT thickness and bulge diameter on oxygen transport and further supported relative ILT thickness as inducing hypoxic conditions [5]. However, fluid-flow is known to affect mass-transport and as a result oxygen distribution [10]. Moreover, luminal recirculation patterns are not considered despite the known perturbation of structural integrity in the AAA during inflammatory response [11]. Furthermore, slowed luminal blood flow elicits coagulation thus altering the composition, thickness diffusivity of the ILT which is not considered in this study [12].

In extended models, the ILT is considered permeable due to its highly porous canalicular network Vande Geest developed a porohyperelastic constitutive model coupling the solid and fluid component of a porous ILT [13]. The framework of the model was designed to investigate the relationships between stresses, strains and interstitial fluid velocities [13]. Darcy's law was used to obtain relative fluid velocity values influenced by permeability and pressure gradients within the porous media [13]. The model excludes diffusion driven transport and results are representative of convention transport [13]. Despite an expanded model including a porous domain, hemodynamics of the lumen is neglected once more. In another porous model, Polzer uses an elastic solid skeleton with interconnected pores of liquid to represent the thrombus. The poroelastic properties of the ILT on stress in the aneurysmal wall is represented by Biot's theory at quasi-static conditions [14]. The finite element model was successful in characterizing blood pressure transform into wall tension [14]. However, increasing pressure due to blood flow was not considered [14]. Thus, the variability of wall-strength along the aneurysm due to hypoxia was also neglected [3]. Some regions of the aneurysm may experience peak stress but greater wall strength [3]. In contrast, weakened regions may rupture under a lower stress threshold. Thus, inclusion of hemodynamics within the lumen in both studies will help quantify the effects of fluid-flow.

In one of the few studies that models mass-transport in an AAA, a patient specific geometry is used. For example, Sun developed coupled fluid-dynamics equations with convection-diffusion equations incorporating hemodynamics and mass-transport in an expanded fluid-wall model [15]. However, using patient-specific geometries fails to provide a sensitivity analysis that incorporates physiological meaningful parameters and minimizes the degree of uncertainty between input and output as opposed to a more simplified model. As a result, a

sensitivity test of an idealized, axisymmetric geometry will provide a more thorough analysis. This is especially true for parameters such as ILT oxygen diffusivity and oxygen consumption that cannot be obtained experimentally.

Thus, the objective of this dissertation is to develop an idealized computational model of AAA with a multifaceted parametric study designed to characterize oxygen localization and velocity streamlines in the lumen to project recirculation patterns. The computational framework utilizes a fluid-wall model with three domains the lumen, ILT and arterial wall with an idealized axisymmetric 3D geometry. Fluid dynamics equations are then coupled with advection-diffusion-reaction equations that model the transport of biomolecules in AAA and their interaction with the arterial wall living tissue. Hemodynamics of luminal blood flow is modeled by the Naiver-Stokes equations. Thus, the model provides quantitative velocity field vectors and qualitative streamlines in the lumen during data post processing. Moreover, oxygen concentration contours are derived from the mass-transport equations.

A sensitivity analysis of physiologically meaningful variations of model parameters was then performed to investigate their effect on oxygen transport within an AAA. Our model incorporates several parameters for assessing the biomechanical environment inside the AAA including kinematic diffusivities of oxygen in the tissue, rate of oxygen consumption in the arterial wall, geometry and the Vaso Vasorum (VV). Primarily, different ILT geometries derived from Vorp's study [5] were used to determine the effect of geometry on oxygen localization. The ILT has already been proven to create hypoxic conditions [3, 16, 17]. As a result, changing ILT thickness will quantify the extent that the ILT has on oxygen localization and identify non-sensitive geometries optimizing future models. The next model parameter that will be discussed is the effect of the VV. The adventitial vasa vasorum supplies additional oxygen to the infrarenal

artery by perfusion [18]. Poor distribution of the VV has been observed in the abdominal aorta as compared to other regions in the vessel such as the thoracic aorta [19]. Moreover, hypo fusion of oxygen through the VV how been shown to result in tissue ischemia [20]. More poorly oxygenated ischemic tissue has been measured in the aneurysmal bulge compared to the proximal neck of the aneurysm [21]. As a result, a range of values is used to determine the VV's role in oxygen localization. The purpose of this range is two-fold: firstly, it quantifies the potential of the VV to minimize aneurysmal pathogenesis through supplemental oxygen and secondly considers values representative of a poorly vascularized AAA. The influence of the VV is modeled by the partial pressure of oxygen in the exterior of the model. The final parameter discussed is the diffusivity of the ILT. A range of values less than the kinematic diffusivity of oxygen in the blood to several higher order of magnitudes is considered. The composition, age and thickness of the ILT affects diffusivity. Thus, this range of values is able to account for meaningful values of low and high diffusivities.

This dissertation is as follows: Chapter 2 details the construction of a computational model to simulate the biomechanical environment of an AAA. Each subsection of chapter 2 will act to dissemble the model and provide necessary computational framework. 2.1 defines arterial domains and dimensions, 2.2 defines hemodynamic and convection-diffusion equations. In section 2.3 we detail boundary conditions and parameters, at section 2.4 discuss how the solver generates solutions. Chapter 3 displays a baseline model defining oxygen concentration relative to other cases. In chapter 4, we analyze results of model physical parameters including ILT and wall oxygen diffusivity, effect of the vasa vasorum, arterial geometry, reaction rate and flowrate input. In chapter 5, we discuss results in which certain parameters display a greater effect on oxygen localization and future directions.

Chapter 2 – Computational Model and Methods

In this chapter, we detail the development of a computational model to simulate mass transport and hemodynamics within a 3D axisymmetric AAA. First, we assign model governing equations and parameters used to predict biomechanical behavior. Second, we define the geometry and arterial mechanics of an AAA comprised of an ILT. Third, we generate a mesh composed of discretized elements and nodes used to provide solution vectors. Fourth, we define boundary conditions and assign material properties to three different domains the lumen, ILT and arterial wall. Moreover, we discuss the application of governing equation in ANSYS ICEM CFD software. Lastly, we use a numerical solver in the software program ANSYS to generate 3D and 2D visual plots of oxygen concentration contours and velocity streamlines. The solution vectors are then exported from ANSYS to excel where each case is plotted to obtain local oxygen concentrations.

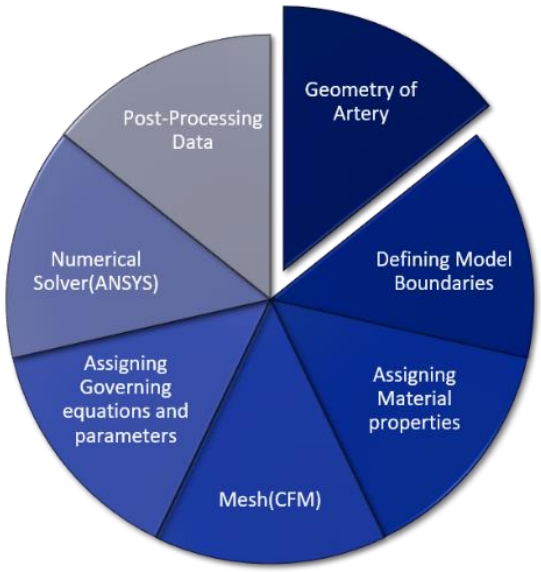

Figure 1 Different components for creating a computational model. The diagram summarizes each component of the computational framework. Each part is necessary in generating a realistic simulation of an AAA.

2.1 *Arterial Dimensions*

Primarily, we define the dimensions of the arterial model. We present a cross-section of the 3D model on the XY plane as a simplified schematic with all 3 domains (**Figure 3**). The length of the vessel is represented by L = 24 cm. The apex of the bulge is at half of the vessel length. This apex represents the bulge diameter (BD) which is equal to 7 cm. The ILT and wall are assigned thickness values of 1.5 cm and 0.5 cm respectively. These metrics were used to define a comparative baseline model consisting of an AAA with a thick ILT. To obtain results for geometry sensitivity analysis the bulge diameter was modified to include dimensions from 5-7 cms and ILT thickness was modified to include 0.5-1.5 cm for the remaining cases. The radius of the vessel was defined at R = 1 cm. Each domain and boundary interface were further clarified in **Figure 3**. The volumes of each domain were assigned by omega (**Ω**) with their respective subscript, *w* for the wall, *ilt* for the ILT and *l* for the lumen. The interfaces between boundaries were defined by gamma (Γ) using the same subscripts. Each domain was assigned specific material properties to replicate the biomechanical environment of the AAA. Such properties mainly affect density, oxygen diffusivity and viscosity. Material properties are further defined in **Table 1**. Blood was used to define fluid-flow within the lumen. The ILT and wall are modeled as solid, rigid structures and are assigned their respective properties.

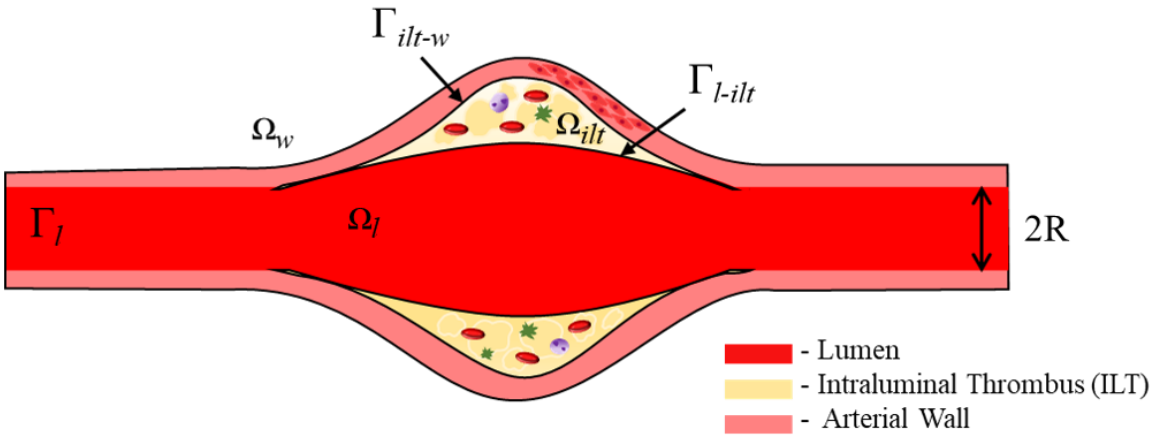

Figure 2 Schematic of the axisymmetric AAA. Omega repersents volumetric domains (ω).

Gamma represents the interfaces between each boundary (Γ).

Table 1 Summary of material properties

	Blood	**ILT**	**Wall**
Thermodynamic state	Liquid	Solid	Solid
Molar mass	18 [kg/kmol]	18 [kg/kmol]	18 [kg/kmol]
Density	1060 [kg/m^3]	1000 [kg/m^3]	1000 [kg/m^3]
Dynamic viscosity	0.003 [Pa s]	6.54e^{-4} [Pa s]	6.54e^{-4} [Pa s]
Reference temperature	37 [C]		
Reference pressure	0 [mmHg]		

2.2 Mathematical model

In the mathematical model, governing equations are assigned to three different domains: the lumen, the ILT and the wall. We first discuss hemodynamic equations assigned to the lumen. The abdominal aorta is a large vessel with a large diameter. As a result, we make the assumption that blood flow resembles an incompressible, Newtonian viscous fluid with steady laminar flow. Fluid-flow is modeled mathematically by the Naiver-Stokes equation:

$$\rho_l(\boldsymbol{U_l}\,\nabla\boldsymbol{U_l}) \;=\; \nabla.\boldsymbol{\sigma_l} \tag{1}$$

$$\nabla.\boldsymbol{U} \;=\; 0 \tag{2}$$

In these equations, $\boldsymbol{U_l}$ represents the fluid velocity field, ρ_l represents blood density and $\boldsymbol{\sigma_l} = -p_l\boldsymbol{I} + 2\mu_l(\boldsymbol{U}_l)$ represents the fluid Cauchy stress sensor where blood viscosity is μ_l and fluid pressure is p_l. The symmetric fluid velocity field vector is represented by $(\boldsymbol{U}_l) = \frac{1}{2}(\nabla\boldsymbol{U}_l + \nabla\boldsymbol{U}_l{}^{\mathrm{T}})$. Subscripts *l, ilt* and *w* are used to represent blood flow in each domain respectively. The hemodynamic equations are then coupled with diffusion equations to generate convection-diffusion equations in the lumen:

$$\rho\,\boldsymbol{U_l}\,\nabla\cdot C_l - \rho\,D_l\,\Delta C_l = 0 \tag{3}$$

Equations were coupled to investigate the effect of fluid flow on oxygen transport during steady state. The density of blood was represented as ρ and diffusivity of oxygen D_l.

Oxygen transport toward the exterior of the model was then considered. A diffusion equation was used to model oxygen transport through a nonreactive, impermeable solid domain:

$$-D_{ilt}\nabla^2 C_{ilt} = 0 \tag{4}$$

This equation is used to represent the gradient of oxygen concentration with respect to diffusivity in a uniform medium. The localization and concentration of oxygen was relative to diffusion in

the ILT. The coefficient of ILT diffusion is represented by D_{ilt}. To model smooth muscle cell oxygen consumption of the arterial wall, the equation was extended to contain a reaction term:

$$-D_w \nabla^2 C_w = r C_w \tag{5}$$

The coefficient of diffusion is represented by D_w. The reaction term is defined by rC_w and the reaction rate by r [22]. The term relates to oxygen consumption due to cellular metabolism.

2.3 *Boundary Conditions and Parameters*

In this section, we detail the model's boundary condition and parameters. We start by defining the inlet of the lumen. The concentration at the inlet of the model is set to a constant value:

$$C = \alpha(pO_2) = 5.12 \cdot 10^{-3}\ [kg\ m^{-3}] \tag{6}$$

This value was derived from the molar mass of oxygen under the assumption that the partial pressure of oxygen was 100 mmHg throughout the inlet. The oxygen-carrying capacity of hemoglobin is neglected as the pO_2 equates to the concentration of unbound oxygen molecules. The flowrate in the inlet is representative of resting conditions and is matched to physiological meaningful Reynold numbers that reflect the viscosity of blood. The directionally and flow pattern in the lumen of the model are further defined (**Figure 2**). The velocity profile at the inlet is defined by the following equation:

$$\boldsymbol{U}_{inlet} = 0.235 \left(1 - \left(\frac{y^2+z^2}{1\cdot10^{-4}}\right)\right)[m\ s^{-1}] \tag{7}$$

An average velocity of 0.235 m/s was obtained from flowrates reported by [23, 24]. The vessel radius is represented by $1\cdot10^{-4}$ m and the specific dimensions of the inlet are defined by the y and z values to obtain a velocity vector $\boldsymbol{U}_{inlet}$. To model human blood flow specifically, fluid density was defined by *pl* = 1050 kg/m and viscosity 0.0035 kg.ms. Boundary conditions were used to

specify flow and oxygen transport modeling flux in certain locations. The Neumann boundary condition was used to model oxygen flux at all outlets. Furthermore, this condition restricted re-entry of oxygen once through the boundary. This was done to represent oxygen transport into tissue. To represent the vasa vasorum, a partial pressure of 50 mmHg was assigned using a Dirichlet boundary condition defined at the exterior of the wall [7]. A boundary wall type was defined at the inlet and outlet of the wall preventing the exit of oxygen. To define the interior of the model, a relative flux of oxygen between the *ilt-w* and *ilt-l* was defined by a conservative flux condition. A no-slip condition was also used to define the interfaces between the *l-w* and *l-ilt*. These conditions were based under the assumption:

$$\begin{aligned} C_l &= C_w && in\ \Gamma_{l-w} \\ C_l &= C_{ilt} && in\ \Gamma_{l-ilt} \\ C_{ilt} &= C_w && in\ \Gamma_{ilt-w} \end{aligned} \tag{8}$$

These conditions were used to ensure appropriate oxygen localization and increase the accuracy of the model.

The parameters of the convection-diffusion equations are defined by kinematic diffusivity coefficients. The diffusivity coefficient of the wall and ILT are $D_l = 1.34 \times 10^{-9}$ m^2/s and $D_w = 1.08 \times 10^{-9}$ m^2/s respectively (**Table 2**) [15, 25]. For the arterial wall, the additional parameter of the reaction term was defined. The reaction term was determined under the assumption that the volume flux of oxygen is completely consumed by the smooth muscle cells (SMC) of the arterial wall using the equation:

$$J_w = V'_{crit}\, N = r\, h\, C \tag{9}$$

V'_{crit} represents oxygen consumption of an individual SMC. The number of SMC in the arterial wall is represented by N. A linear decrease of SMC counts per unit centimeter of the arterial wall

occurs from the inlet and outlet toward the apex of the bulge. The arterial wall's thickness is defined by h = 1.0 x 10^{-4} m. The reaction rate r = 8.4 x 10^{-3} s^{-1} was taken from a previous study [23]. This value was deemed appropriate as calculations utilizing the initial oxygen concentration derived a comparative value.

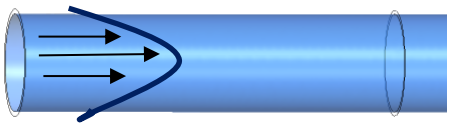

Figure 3 Schematic of inlet flow condition. The unidirectional, laminar flow of the inlet is modeled. The curved line and arrows are used to represent the parabolic velocity profile.

Table 2 Summary of relevant parameters.

Variable	Term	Coefficient
Concentration of Oxygen at Inlet	C_l^{in}	5.12x10^{-3} kg/cm^3
Inlet Oxygen Partial Pressure	PO_{2Inlet}	100 mmHg
Kinematic Diffusivity of Oxygen in ILT	D_{ilt}	1.34x10^{-9} m^2/s
Kinematic Diffusivity of Oxygen in Wall	D_w	1.08x10^{-9} m^2/s
Reaction Rate	r	8.4x10^{-3} s^{-1}

2.4 -*Computational Solver*

In this section, we detail the final component to our computational framework. We use ANSYS CFX Workbench (v.19.3 ANSYS Inc., Canonsburg, PA, USA) a software tool for computational fluid dynamics (CFD) with multiphysics applications. For our particular model, a fully coupled strategy is implemented to solve all equations simultaneously. Geometry was represented by a tetrahedral mesh composed of 1.5 million elements discretized by a cell based finite volume method (**Figure 3**). Nodal components were evaluated to obtain solution vectors. To solve the equations simultaneously, a monolithic linear system that embraces all degrees of freedom was used. Furthermore, LU incomplete factorization was used as a preconditioner to

accelerate the iterative solution process (**Figure 4**). Pericard iterations were used to construct a sequence of functions that would ultimately yield a solution with a convergence criterion of 10^{-6} to achieve steady state. This was used to linearize the convection term in the Naiver-Stokes equation. The pressure variable in the Navier-Stokes equations is evaluated at the same nodes of the velocity field. An algebraic multigrid method is used to solve the system of equations that contain varying levels of discretization and functional behavior. This method is used as a complement to LU factorization generating a smoother convergence. The remaining convection terms were discretized by an upwind method, a solution sensitive finite difference scheme. The Laplacian operator from the fluid and momentum equations was approximated by a center scheme. Simulations were performed Numerical simulations have been performed on parallel CPUs using a 5-Core Intel CPU, 32 GB RAM at Duquesne University.

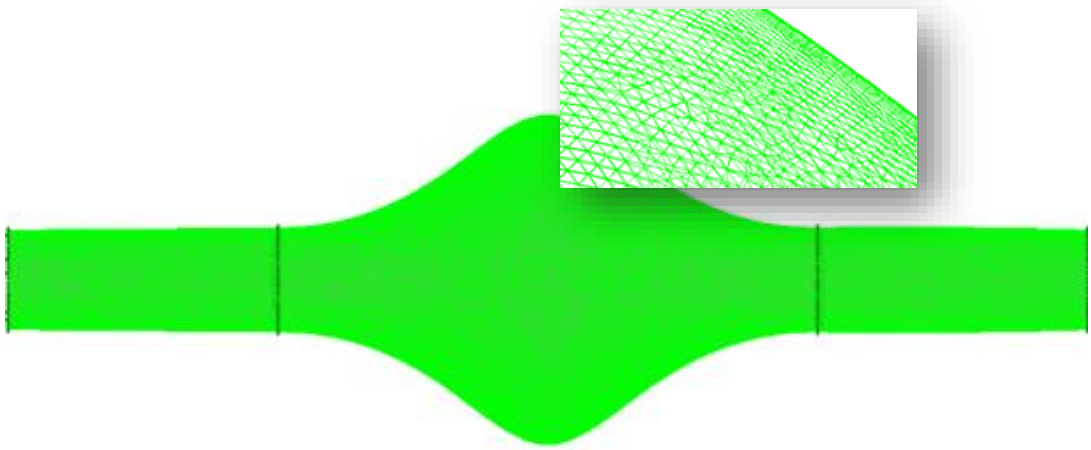

Figure 4 Computational mesh for AAA model. Generated by ICEM and imported to the ANSYS workbench.

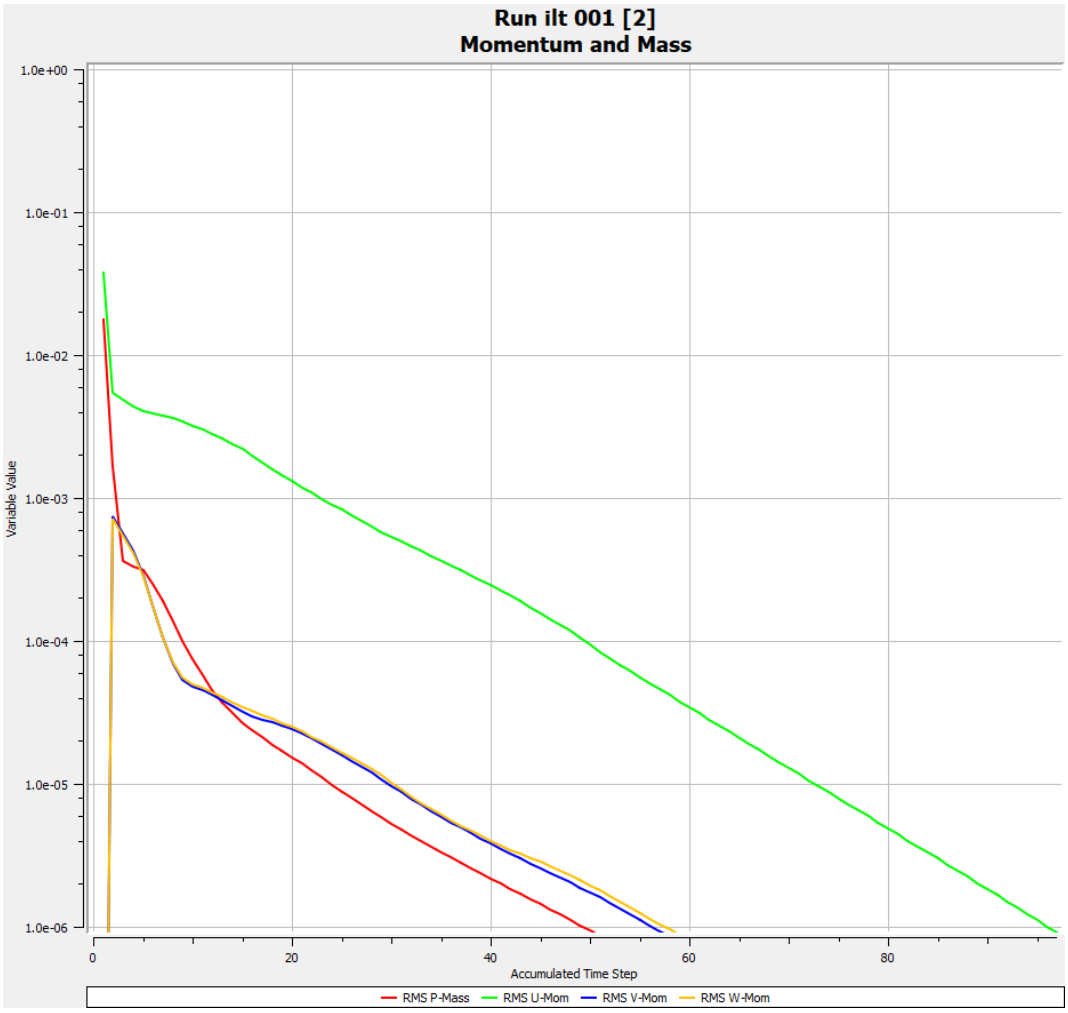

Figure 5 Convergence plot using residual values. A graphical representation of function variables for momentum and mass being iteratively solved until a steady state condition is achieved at a convergence of 1.0 x10^{-6}. Variables are defined by the figure legend.

Chapter 3 – Results for Baseline Case

In this section, we discuss the results of a baseline model. Parameters specific to this case were outlined in the previous section. Simulations that manipulate parameters of interest will be relatively compared. Thus, our results will focus on the spatial distribution of oxygen concentration represented by a color scale. Blue indicates hypoxic conditions and red represents oxygen rich concentrations with mid-range values falling in between this color scale. Supplemental plots of luminal streamlines, velocity and pressure will also utilize this color scale and provide data on blood flow.

We start by decomposing the simulation into each domain beginning with the results of the lumen. A cross-section of the lumen oriented on the XY plane of the 3D plot is shown (**Figure 6**). The lumen was found to show a uniform oxygen distribution as indicated by the red coloring and lack of variation. The initial concentration is equivalent to the maximum concentration of the color scale and is consistent throughout the lumen. This implies consistent oxygen availability throughout the interface between the *l-ilt* and *l-w* for transport. The minimum concentration of oxygen on the scale is equivalent to the partial pressure of the vasa vasorum and has no effect on the interior of the lumen.

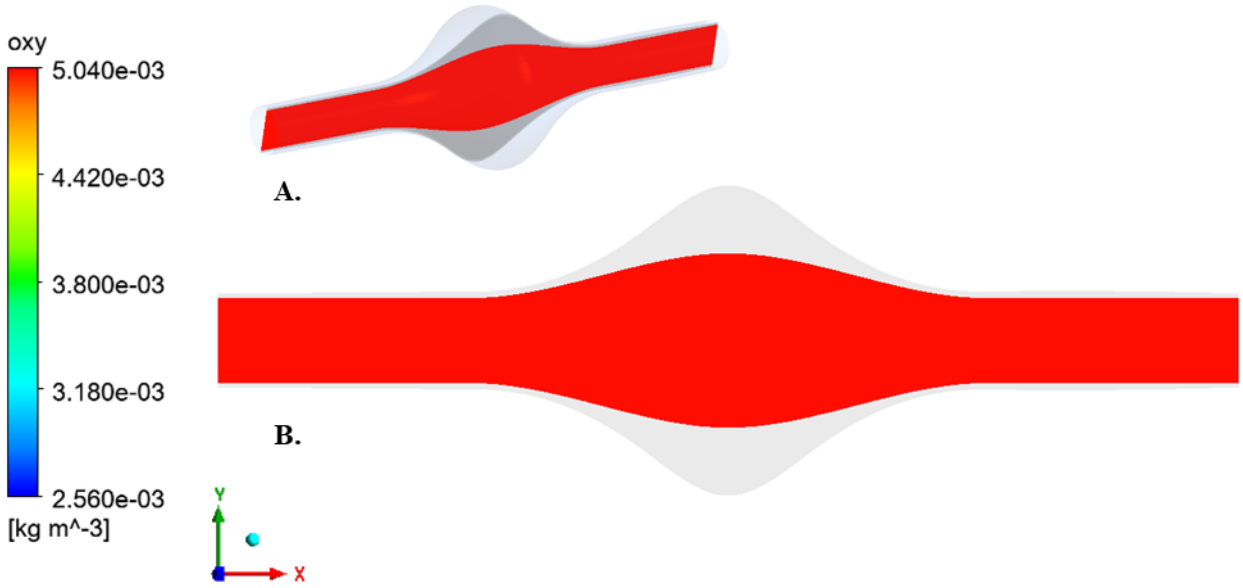

Figure 6 Luminal oxygen concentration. (A) A shadow of the 3D geometry is shown to visual the cross-section of the XY plane. (B) Lumenal oxygen concentration shown with the remaining domains of the ILT and wall outlined in grey.

Secondly, a cross-section of the ILT shown on the same plane and perspective of the lumen showed variability within a local color scale. The maximum and minimum of the scale represent variables solved in the current timestep of the ILT only. The interior of the ILT is dark orange and quickly fades throughout the color spectrum until a thick layer of dark blue is shown (**Figure 7**). This represents a steep decrease in oxygen concentration and a large step in the function. As one would intuitively presume, thick bands of color on the contour plot represent large changes in oxygen concentration and thin bands represent small changes in oxygen concentration emphasizing the importance of spatial distribution. To further explain, thick bands indicative of hypoxic conditions show oxygen is able to penetrate the ILT only to a certain extent. Thus, there is a greater need for supplemental oxygen in the exterior of the artery.

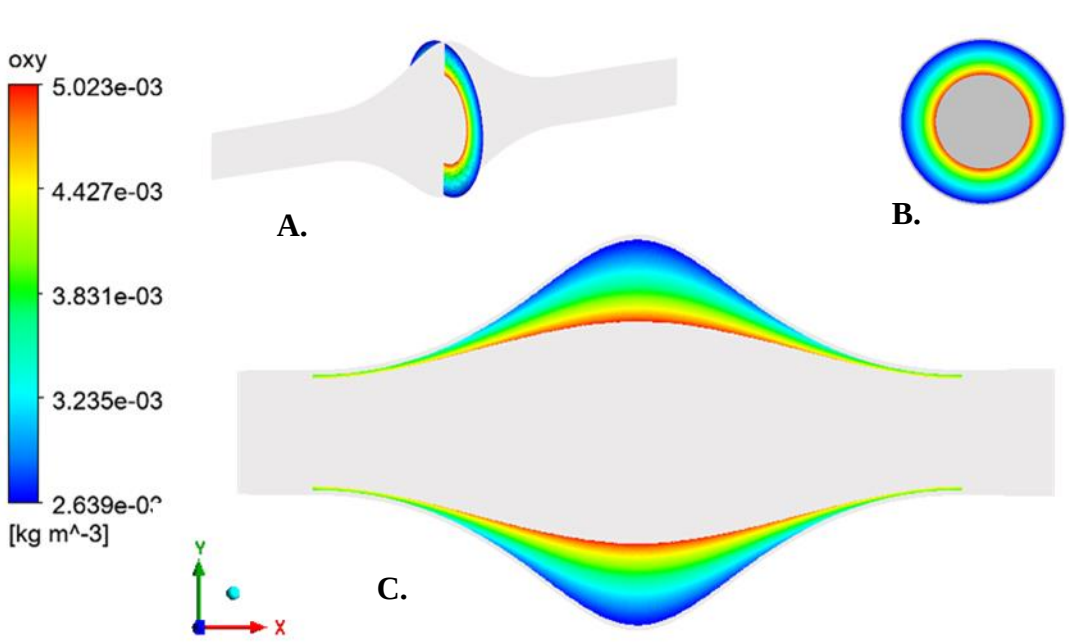

Figure 7 Local ILT oxygen concentration. The scale is adjusted to contain the local minimum and maximum variables of oxygen concentration in the ILT. (A) The spatial distribution of oxygen concentration in the XY plane of the ILT represented by a color scale. Lumen and wall outlined in grey. (B) Indicates the orientation of the ZY plane with respect to a grey plane XY cross-section (C) Slice of ILT concentration shown on ZY plane.

The arterial wall is then considered from the same perspective. A local color scale is used to show the full color range of the specific domain. The bulge shows no oxygen concentration apart from the supplement oxygen of the vasa vasorum. The healthy tissue represented at either end of the bulge shows evidence of oxygen transport. The healthy tissue is shown to have a broader spectrum of color as compared to the uniform dark blue of the bulge **(Figure 8**). This shows the obstruction of oxygen transport in the aneurysmal bulge due to the presence of an ILT.

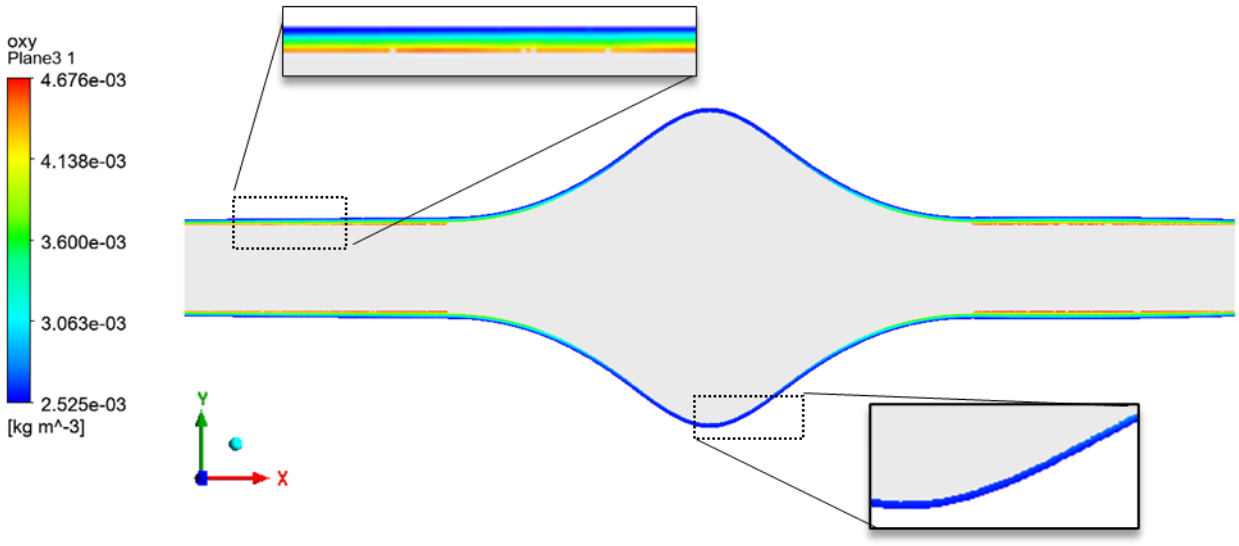

Figure 8 Local arterial wall oxygen concentration. The arterial wall is shown in the XY plane with luminal and ILT domains represented by a gray shadow. Zoomed in panels of the arterial wall are used to show the difference in oxygen concentration between healthy and diseased tissue.

After viewing the ILT and wall domains at a local level of color distribution, a global scale using the maximum inlet concentration and external concentration supplied by the vasa vasorum was used to compare domains simultaneously. A volumetric rendering of the model was used to represent the color distribution with respect to a 3D scalar field (**Figure 9A**). This was done to visualize the orientation of the vessel from a 3D perspective. A XY cross section of the 3D model was used to visualize oxygen contours from a 2D plane (**Figure 9B**). Results showed the ILT with a lower oxygen concentration at the *l-ilt* interface as opposed to the local scale. However, throughout the length of the vessel the appearance of oxygen concentration at *l-ilt* interface is shown to be a constant, mid-range yellow both at the bulge and healthy tissue. Variation begins at the bulge and is further supported to show a greater spatial distribution of hypoxic zones in between contours. This is shown in the three YZ slices of oxygen concentration

at the apex of the bulge, beginning of the bulge and at the start of the vessel (**Figure 10**). Thus, a direct correlation between ILT thickness and hypoxic regions is observed.

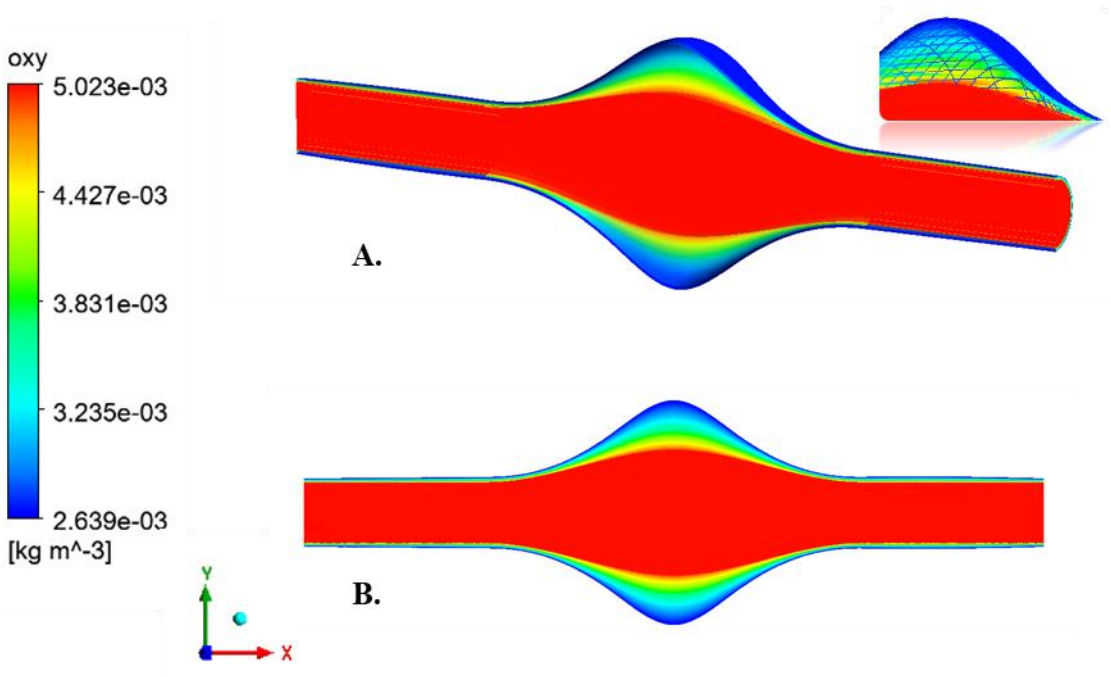

Figure 9 Comparison of oxygen concentration across 3 domains. (A) Volumetric rendering of oxygen concentration of the 3D model cut in half across the luminal domain. Zoomed in panel used to show mesh lines of the model (B) A 2D contour plot of all 3 domains in the XY plane.

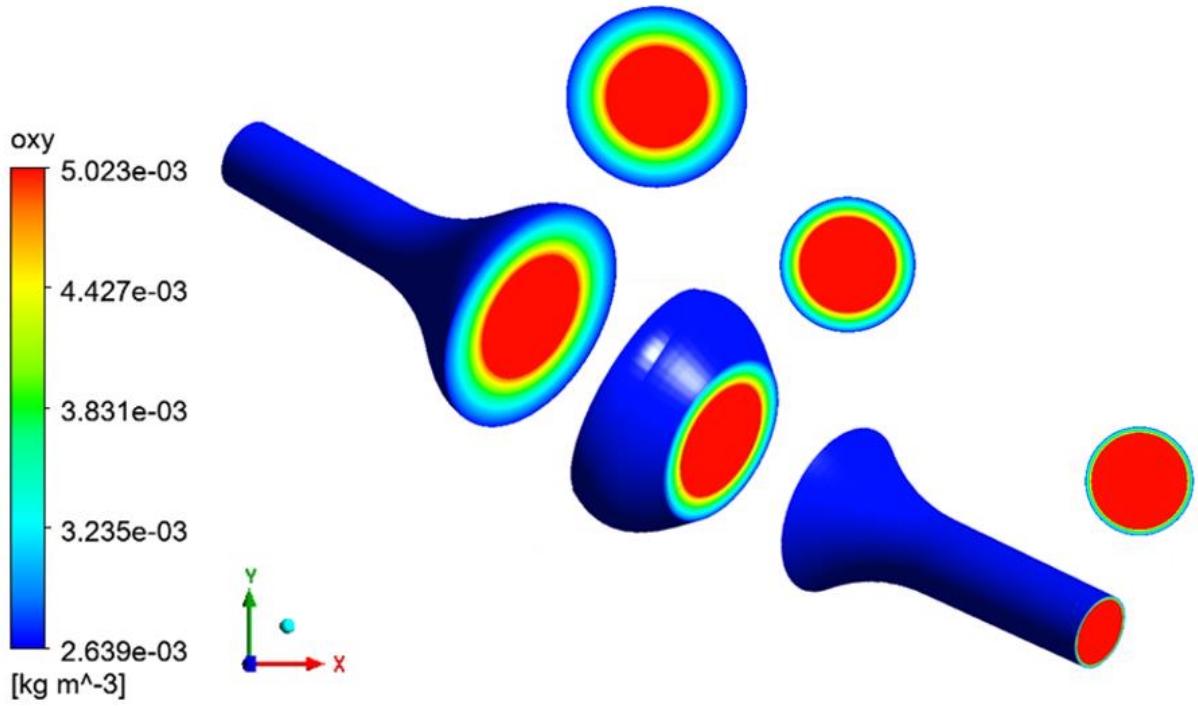

Figure 10 3D model of oxygen concentration sliced into 3 parts. Oxygen contours are shown in the 3D model of the artery. Three slices of YZ planes at different sections are shown.

As mentioned previously, blood flow elicits coagulation and potential advancement of pathogenic mechanisms within the aneurysmal bulge altering the composition of the ILT. Thus, we observe the results of blood flow within the luminal domain. Primarily, a color scale is used to show deceleration and acceleration of velocity based on specific areas of the vessel. The parabolic, laminar flow of the vessel is shown at the inlet of the vessel. The centerline velocity is indicated by red and the lowest velocity is found along the vessel wall as indicated by the darkened color-scale (**Figure 11A**). To further understand velocity, **Figure 11B** shows a pattern of streamlines correlating with the trajectory of blood flow. The expanded sac of the aneurysmal bulge shows deceleration of blood flow in both the velocity contour plot and the plot of streamlines. The trajectory of the streamlines indicates recirculation zones and distribution of

flow within the lumen. This is due to the expanded diameter of the vessel at the aneurysmal sac slowing the velocity of blood flow.

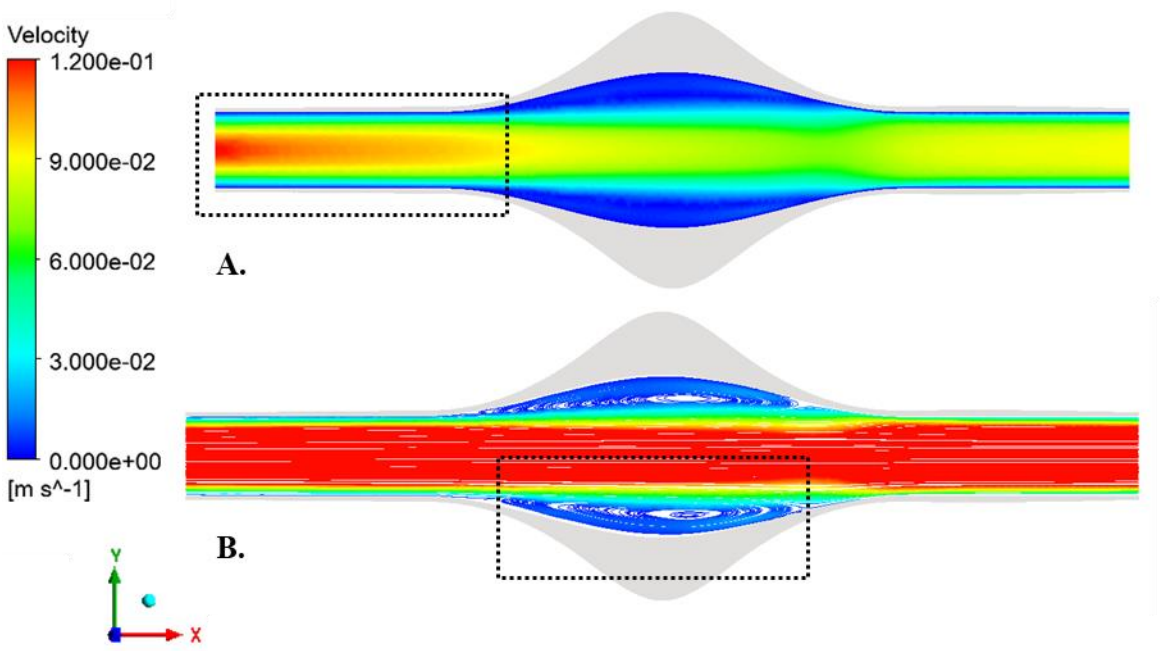

Figure 11 Velocity and streamline contour plots. (A) Velocity contour in the XY plane cut along the luminal domain with remaining domains shown in grey. (B) Streamline contours in the same orientation.

Total fluid pressure within the vessel is then considered. A color distribution of values similar to that of velocity is shown (**Figure 12**). The highest total pressure is found at the inlet resembling the laminar velocity profile. As the fluid dissipates through the vessel pressure is lost. Thus, as you move laterally toward the outlet of the vessel a lower pressure gradient is observed. Furthermore, the aneurysmal sac shows lower pressure values. Pressure profiles can help to characterize the link between hypertension and aneurysmal rupture. Increased blood flow creates a higher-pressure gradient acting on the aneurysmal wall. A non-uniform luminal pressure shows particular areas of the artery experience greater pressure or shear wall stress.

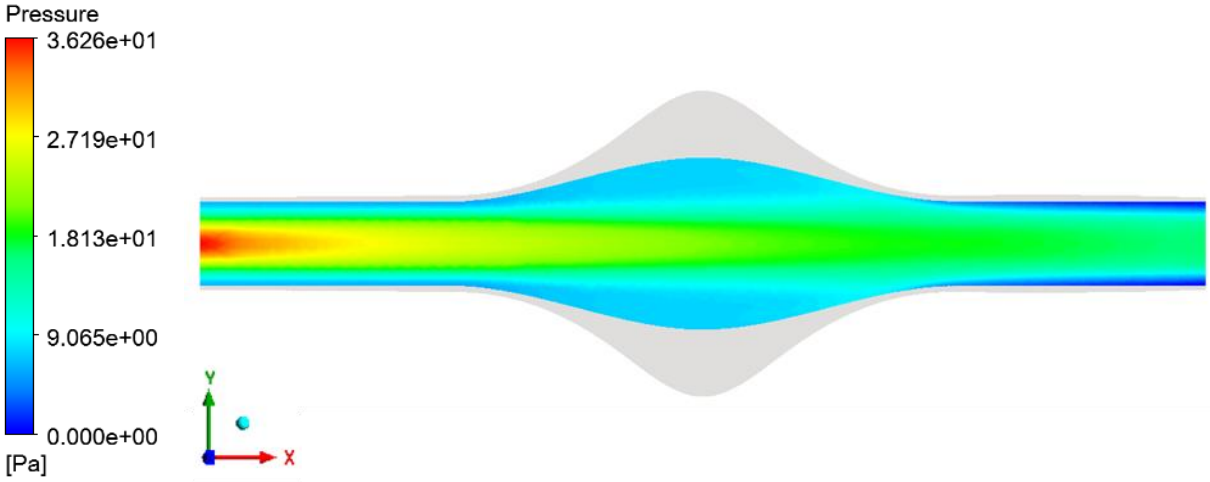

Figure 12 Pressure contour plot. A cross-section along the luminal domain of pressure contours on the XY plane. Wall and ILT are shown in grey.

Chapter 4 – Sensitivity Analysis

4.1 Effect of ILT and Wall Oxygen diffusivity

The abdominal aorta presents a particular challenge in measuring oxygen diffusivity within its tissues. Techniques utilizing microelectrodes to measure oxygen concentration are invasive and mostly rely on animal models [26]. On the other hand, different forms of microscopy utilize the spectral wavelength of the oxygen molecule to derive a particular concentration or utilize oxygen as a quenching molecule characterizing concentration by a reduction in fluorescence intensity both unable to encapsulate heterogeneity of the microvascular environment [26]. To further explain, myoglobin and hemoglobin-oxygen kinetics, PH, and pressure gradients can all affect passive diffusion and microcirculation [27]. Such factors ultimately affect diffusion within arterial tissues. Moreover, lateral changes throughout the vessel can result in varied arterial wall thickness and diffusivity. Thus, diffusivity coefficients that range from the diffusivity of blood and decrease by several orders of magnitudes were used.

Primarily, we list the diffusivity coefficients in the ILT. The baseline diffusivity was chosen at a value $D_{ilt} = 1.34x10^{-9}$ m^2/s. We increased this value by 10 times at $D_{ilt} = 1.34 \times 10^{-8}$ m^2/s an estimate similar to the physiological diffusivity of oxygen within blood. To represent an aged ILT with a dense canicular network, diffusivities 1.34×10^{-10} m^2/s and 1.34×10^{-11} m^2/s were chosen respectively. This represented an exponential decrease in oxygen diffusivity from case 1 to 4. Plots of oxygen contours for each case shown in **Figure 13**. The baseline case was identified in red. The greatest change in diffusivity is seen between cases 1 and 2. Case 1 is shown to contain mid-range values according to the color scheme. The *ilt-l* interface in case 1 shows the lowest oxygen concentration when compared to the other cases. Cases 2-3 showed the maximum oxygen concentration at the interior of the lumen with a gradual decrease in oxygen

concentration towards its exterior. Case 4 showed a thicker hypoxic region and represented the lowest diffusivity of the ILT.

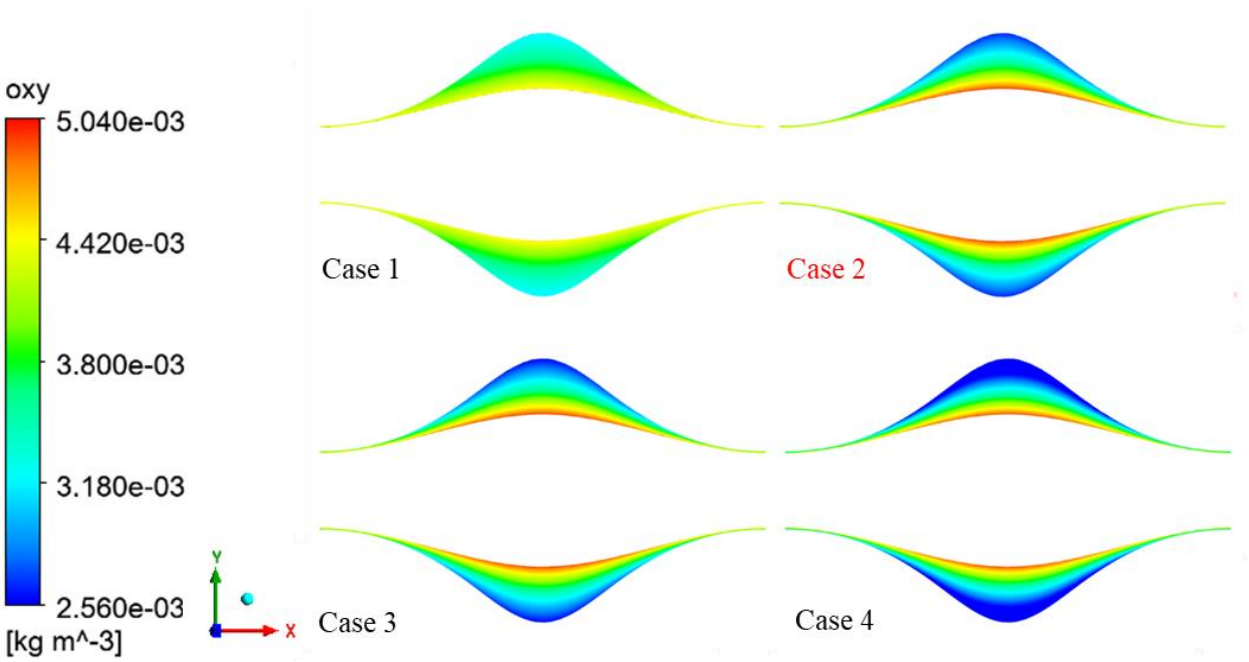

Figure 13 Oxygen contour plots of various oxygen diffusivities in the ILT. Analyzed oxygen concentrations for physiological meaningful diffusivities in the ILT. Cases 1-4 are D_{ilt} = 1.34 $x10^{-8}$ m^2/s, $1.34x10^{-9}$ m^2/s, 1.34 $x10^{-10}$ m^2/s and 1.34 $x10^{-11}$ m^2/s respectively.

To ensure accuracy and provide a quantitative measurement of data values, supplemental plots of oxygen concentrations were derived from each simulation. Beginning from the origin or center point of the model, a line was drawn in the vertical-y direction. Thus, oxygen concentration is measured at various points along a vertical line with unchanging x and z components (**Figure 14A**). This line was drawn at the apex of the bulge to include full ILT thickness. The line appeared to be a constant value slightly greater than 5 x 10^{-3} kg/m^3 until a distance indicating the *l-ilt* interface of 0.02 m was reached. Values of oxygen concentration then

start a rapid decline. Furthermore, steady oxygen concentration values represent the initial, uniform conditions defined at the inlet with a decline in values showing the effect of oxygen transport within the thrombus only. As shown in the oxygen contour plots of cases 2-4, oxygen concentrations in the exterior of the ILT declined. Exact values in the supplemental plots show a decrease in more than half of the original value of 5.12×10^{-3} kg/m^3 to around 2.5×10^{-3} kg/m^3 representative of oxgen supplied by the vasa vasorum. Cases 2-4 showed the same general trend with case 2 showing only a slight difference in oxygen concentration. Case 1 showed a more shallow trend in data with oxygen concentrations at the exterior of the ILT valued around 3.1×10^3 kg/m^3. Thus, quantative data was able to support the initial findings in the oxygen contour plots.

A second line was drawn across the *ilt-w* interface (**Figure 14B**). This was used to show how oxygen concentration changed along the bulge of the ILT. Intuitively, the apex of the bulge should show the lowest levels of oxygen concentration as compared to the proximal and distal neck of the ILT. Thus, ILT thickness is used to provide a trend in oxygen concentration within some cases of relative diffusivity. Unlike the first line, data points are taken along the x-axis through the entire length of the thrombus. Data in cases 1 and 2 were shown to resemble an upside-down parabola. This represents the direct relationship between oxygen concentration and the symmetric bulge of the thrombus. However, once diffusivity was decreased in cases 3 and 4 the parabola broadened respectively until results showed a flat line. This means oxygen concentration varied along the *ilt-w* interface up to a certain extent of diffusivity. Demonstrating the ILT as more impenetrable barrier to oxygen diffusion in those cases. Case 1 was unique in that it had a very high-level of diffusivity similar to that of a fluid (blood). Thus, it makes sense that when compared to the other cases complete hypoxia was not seen within the exterior of the

ILT. Results showed case 1 oxygen concentration at 0.12 m or the apex of ILT thickness was around 3.1x 10^{-3} kg/m^3. Cases 3-4 showed oxygen concentrations at around 2.5x 10^{-3} kg/m^3. Thus, values were shown at 50% initial oxygen concentration correlating with hypoxia.

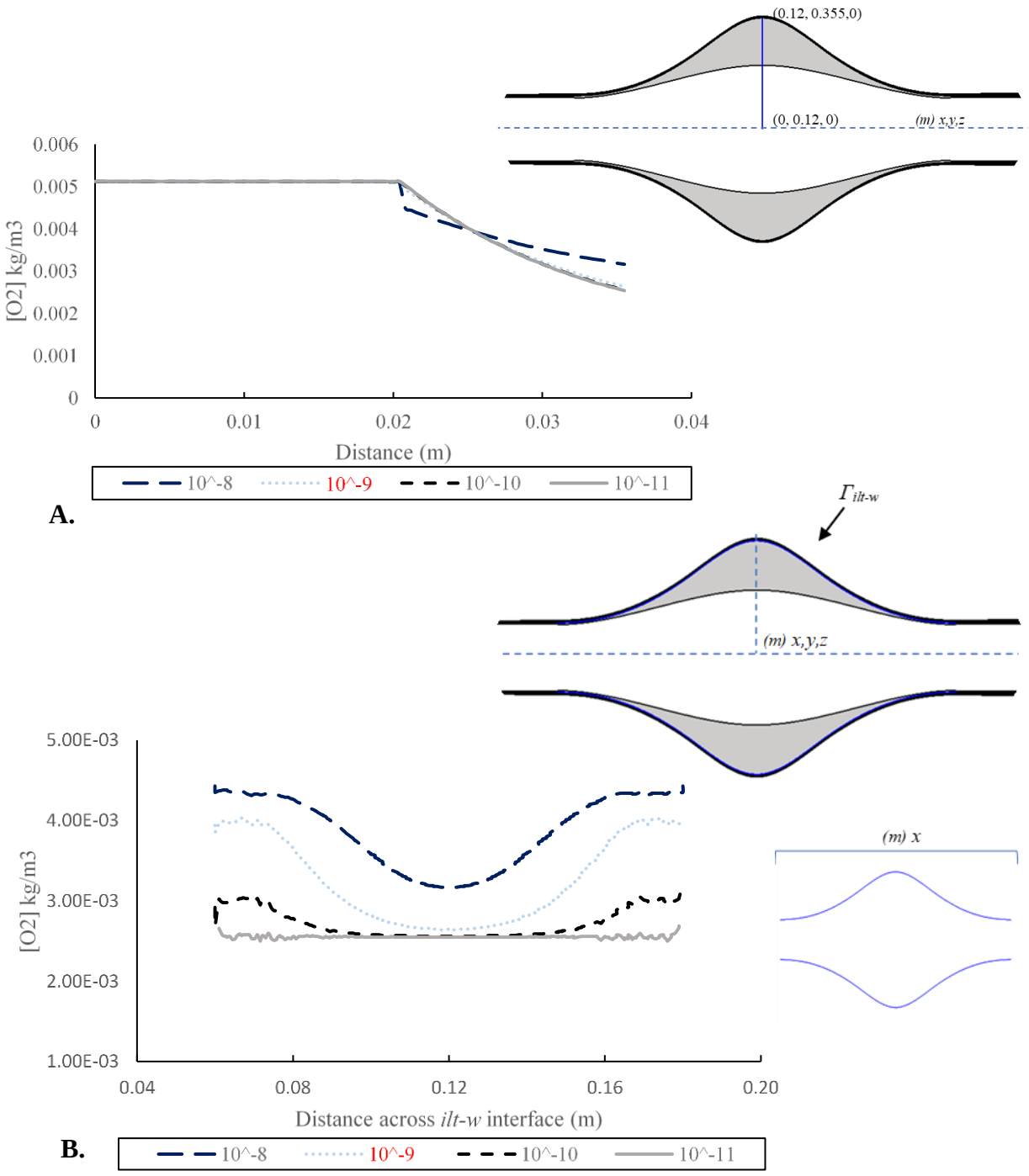

Figure 14 Quantitative plots of oxygen concentration for ILT diffusivity. (A) Oxygen concentration along a vertical line in cases of varying ILT diffusivity. Top Right: Further defines location of derived data points. (B) Values taken from *ilt-w* interface in all cases. Bottom right: shows the outline and location of additional data points.

Using the same protocol and method of interpretation, wall diffusivity was then analyzed. An exponential increase in oxygen diffusivities within the arterial wall resulted in case 1-4 valued at $D_w = 1.08 \times 10^{-8}$ m^2/s, 1.08×10^{-9} m^2/s, 1.08×10^{-10} m^2/s, 1.08×10^{-11} m^2/s. Similar to ILT diffusivity, the comparative baseline model is defined in red as case 2. Beginning with the highest diffusivity in case 1, we observe mid-range values at the interior of the ILT and minimum hypoxic oxygen concentrations at the exterior (**Figure 15**). Cases 1-2 show dark-blue contours thus indicating the external supplement of oxygen provided by the vasa vasorum is equivalent between cases. However, a maximum concentration of oxygen is observed in the interior of the ILT baseline case. A drastic difference is observed between case 2 and 3 as case 3 displays only highly concentrated values. Case 4 then shows a uniform distribution equivalent to the initial concentration of oxygen. Thus, a negative correlation between wall diffusivity and oxygen concentration within the ILT is observed.

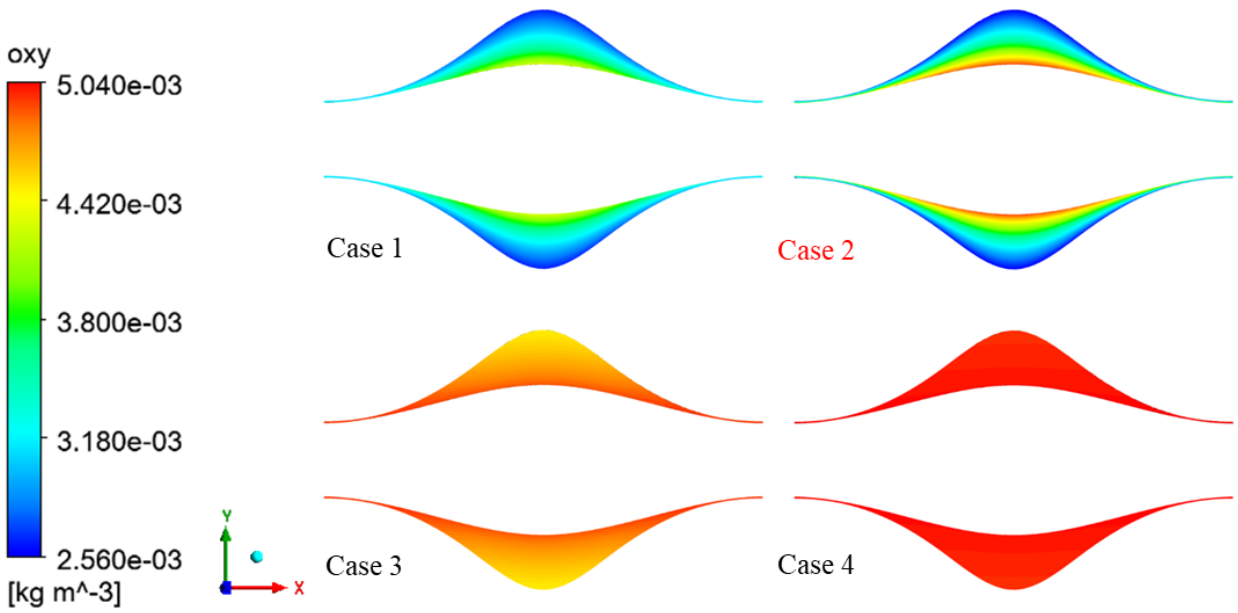

Figure 15 Oxygen contour plots of various oxygen diffusivities in the wall. Analyzed oxygen concentrations for physiological meaningful diffusivities in the wall.

Supplemental plots are again used to quantify data. The same vertical line as the previous parameter is drawn through the ILT. This was used to achieve comparable results between parameters. Exact coordinates and location are shown in **Figure 16**. As seen in the diffusivity of the ILT, the same steady, maximum concentration of oxygen was observed until the *l-ilt* interface is reached. Results show cases 1-2 as following the same general trend with case 2 having a slightly higher final oxygen concentration. Cases 3-4 differ more profoundly. Case 3 oxygen concentration is shown to decrease to a value of around 3 x 10^{-3} kg/m^3. Case 4 is shown as having values nearly exact to initial oxygen concentration. This is represented by the almost horizontal line and trend of the dataset. Moreover, oxygen concentration in the ILT's exterior was shown to be around 4.8 x 10^{-3} kg/m^3 in case 4. Thus, quantitative data was able to support

the qualitative contours of oxygen concentration. However, we were able to observe a slight change in oxygen concentration within case 4 as opposed to the uniform-spatial distribution of red in the contour plot. This showed qualitative data was able to provide a more accurate representation of the dataset between values that differ only slightly.

Using a parallel protocol to the previous parameter, a line was also drawn across the *ilt-w* interface along the x-axis. A visual representation of this is shown in **Figure 16B**. Cases 1 and 4 showed a juxtaposition in results as a flat line is shown at the maximum and minimum oxygen concentrations respectively. Compared to case 4, case 3 shows a decrease in oxygen concentration at the apex of ILT thickness by a factor of 1.4. The corresponding oxygen concentration for case 3 was evaluated at around 3.4×10^{-3} kg/m^3. Cases 1-2 show the same minimum oxygen concentration at the apex of the ILT. However, the proximal and distal areas of the ILT in those cases still indicated a large difference in the gradient of oxygen concentration. As case 2 showed a parabolic trend in data similar to the symmetry of the ILT as opposed to case 1 displaying hypoxic oxygen concentrations throughout the entire interface. This means at a certain diffusivity minimum oxygen diffusion occurred despite geometry. Thus, results from each set of plots indicated the diffusivity of the wall is negatively associated with oxygen concentration within the ILT.

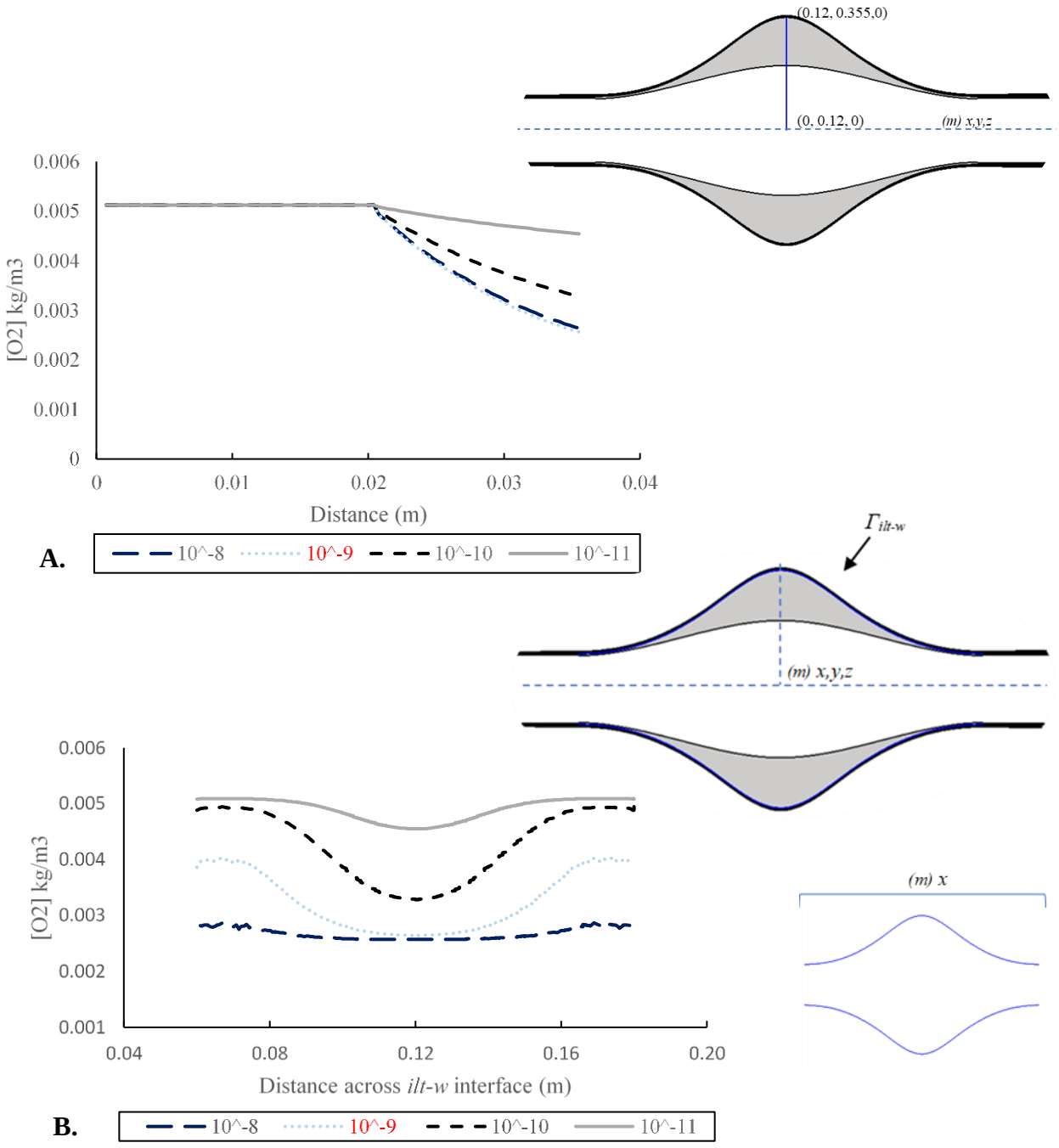

Figure 16 Quantitative plots of oxygen concentration for wall diffusivity. (A) Oxygen concentration along a vertical line in cases of varying wall diffusivity. Top Right: Further defines location of derived data points. (B) Values taken from *ilt-w* interface in all cases. Bottom right: shows the outline and location of additional data points.

In comparing both parameters, an increase in diffusivity of oxygen within the ILT results in a higher concentration of oxygen while an increase in diffusivity of oxygen within the wall results in a lower concentration of oxygen. Diffusivity indicates oxygen molecules can more readily pass through each domain. Thus, when diffusivity decreased in the arterial wall more oxygen was present in the ILT unable to penetrate the medium of the arterial wall. Oxygen diffusivity in the ILT had directly impacted the domain thus oxygen concentration has a direct relationship with diffusivity. However, the model shows that the microvascular environment is more susceptible to diffusivity changes of the arterial wall. Each case showed a large difference in results as compared to ILT diffusivity.

4. 2 Effect of ILT geometry

As it already has been proven that the presence of an ILT significantly decreases oxygen flux to the wall, we look to further support this claim and develop a means to quantify the effect ILT thickness has on oxygen transport. Moreover, to disprove the idea that risk of rupture solely relies on bulge diameter. As a result, we set up four cases that alternate the dimensions of bulge diameter and ILT thickness. A graphical representation was used to describe the relationship of arterial dimensions between 4 cases of varying diameters (**Figure 17**). Bulge diameter ranged from 5-7 cm while ILT thickness ranged from 0.3-1.5 cm using similar metrics derived from a previous study. Bulge diameter was held to a constant 7 cm in cases A-B while ILT thickness was set to 0.3 cm and 1.5 cm respectively. In cases C-D, bulge diameter was set to 5 cm with ILT thickness assigned as 1.5 cm and 0.3 cm respectively. To further define geometry, silhouettes of each case is shown in **Figure 18**. This figure further defines the change in the

shape of the aneurysmal sac within the lumen as bulge diameter is adjusted. Cases D contains a uniform vessel radius ($\Gamma_{l\text{-}ilt}$). In contrast, Case B is shown to have a large aneurysmal sac.

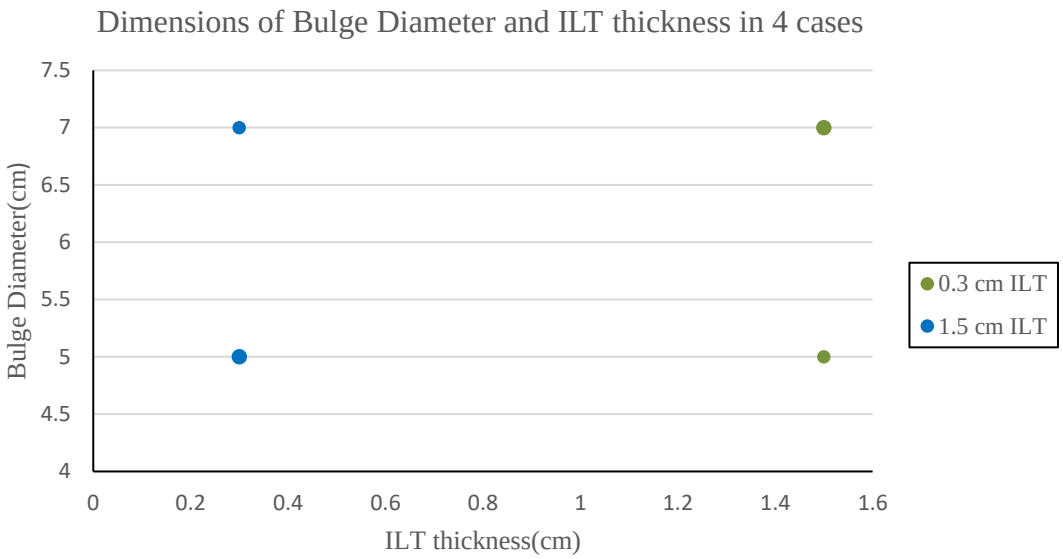

Figure 17 Varying Bulge Diameter and ILT thickness. The relationship between 4 different arterial geometries is shown.

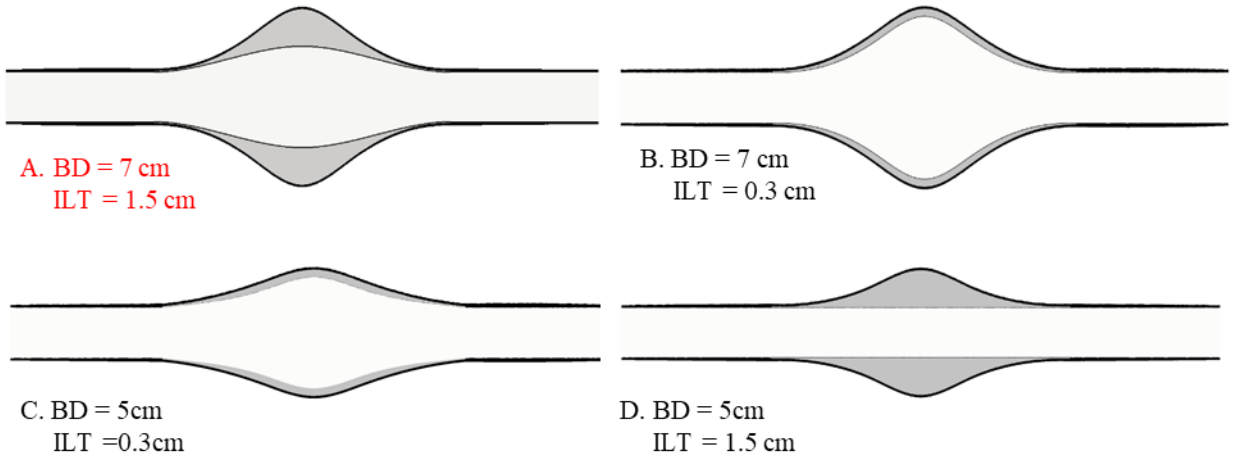

Figure 18 Four silhouettes of AAA geometry. Domains are outlined and bulge diameter (BD) and ILT thickness (ILT) are defined.

A qualitative view of the ILT domain using oxygen contours of each geometry was used to observe changes in oxygen distribution (**Figure 19**). When comparing cases A-B, increased ILT thickness showed a thicker, dark blue hypoxic region. Case B showed mid-range values dominated a majority of the domain as represented by the blue and yellow coloration. Moreover, only a light blue representation of values was able reach the *ilt-w* interface. This indicated oxygen was able to penetrate a thin ILT more readily. When comparing cases A and D whereas only bulge diameter was adjusted, there was no change in the spatial distribution of oxygen contours. A thin ILT with varying budge diameter also showed little effect on oxygen concentration. As a result, ILT thickness had a profound effect on oxygen transport while bulge diameter resulted in no change.

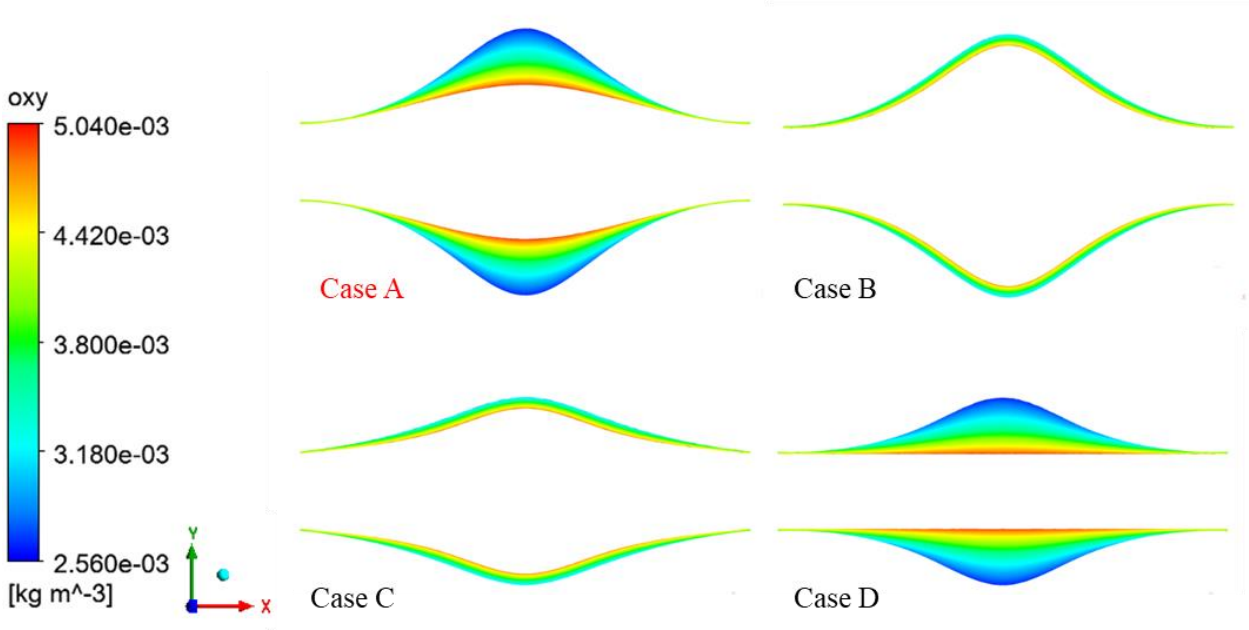

Figure 19 Oxygen contour plots of various geometry. Analyzed oxygen concentrations for varying ILT thickness and bulge diameter. Case A-D are BD = 7cm ILT = 1.5cm , BD = 7cm ILT = 0.3, BD = 5cm ILT = 0.3 cm and BD = 5cm ILT = 1.5 cm respectively.

Supplement plots of oxygen concentration with respect to arterial geometry were used to quantify data (**Figure 20**). The initial concentration of oxygen remained the same until the *l-ilt* interface was reached in each respect case. Due to varying geometry this occurred at different locations. This is shown in **Figure 20A** as oxygen concentration decays at different points between all 4 cases. Trendlines between A and D are associated just as B and D display the same results. This is true in both sets of plots along ILT thickness and the *ilt-w* interface. Oxygen concentration in case A and D with a thick ILT are shown to rapidly decrease and possess lower values overall. Thus, ILT thickness is negatively associated with oxygen concentration while bulge diameter has a minimal affect.

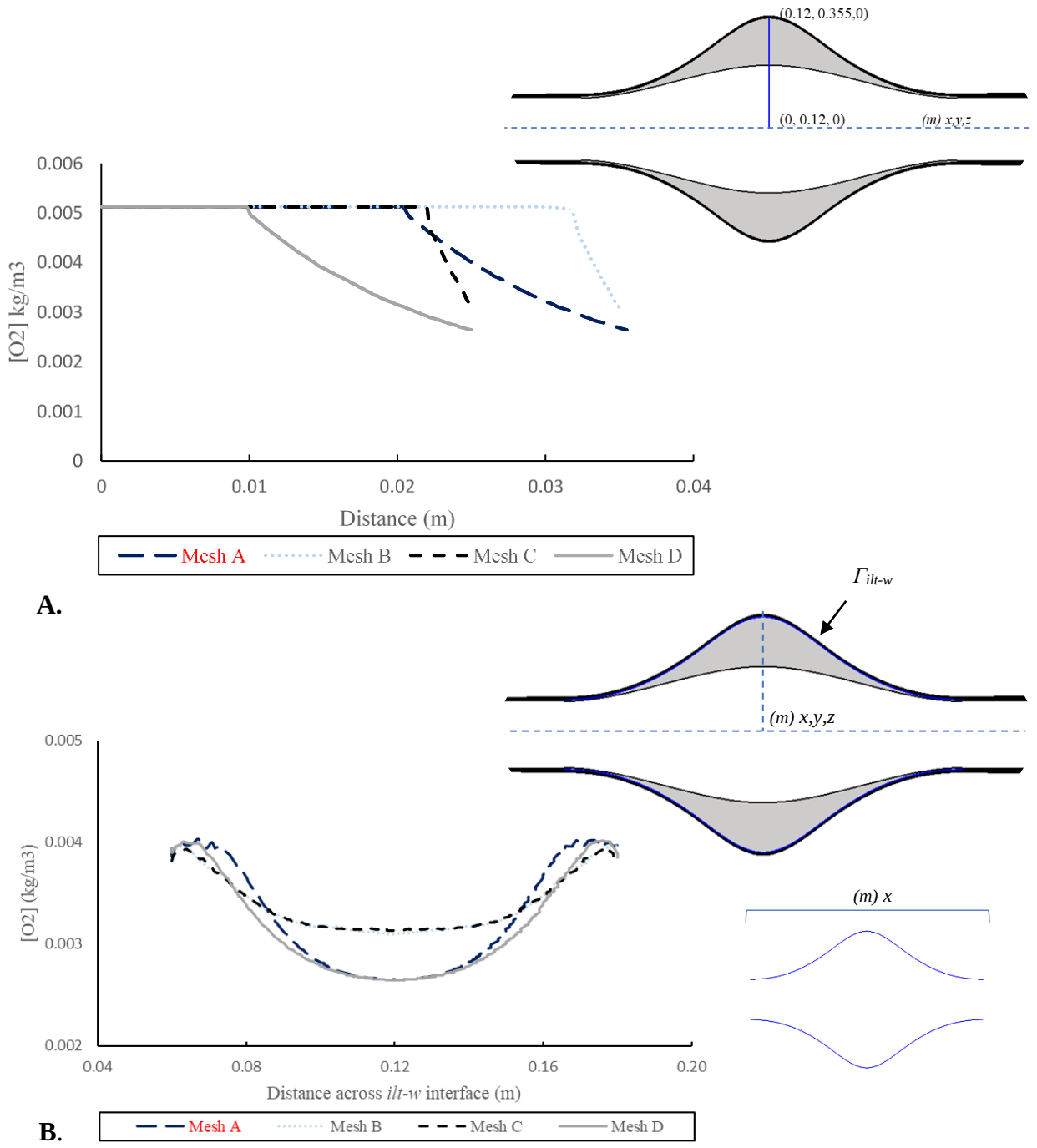

Figure 20 Quantitative plots of oxygen concentration for arterial geometry. (A) Oxygen concentration along a vertical line in cases of varying arterial geometry. Top Right: Further defines location of derived data points. (B) Values taken from *ilt-w* interface in all cases. Bottom right: shows the outline and location of additional data points.

4.3 Effect of the Vasa Vasorum

The Latin term for "vessels of vessels" the vasa vasorum employs adventitial perfusion of external supplements to nourish the arterial wall [28]. Layers of smooth muscles defined as the tunica media of the arterial wall provide vasodilation, vasoconstriction and extra-cellular matrix production [29]. Thus, the role of hypoxic conditions and its effect on smooth muscle cells on the pathophysiology of blood vessels, particularly in the AAA, is brought into question. Previous studies of ruptured AAA have shown hypoxic conditions to be closely associated with aneurysmal rupture [17]. Thus, any abruption to the vasa vasorum such as atherosclerosis, stenosis and injury could potentially deplete the arterial wall of necessary oxygen. The abdominal aorta is particularly susceptible as it is more poorly vascularized when compared to the thoracic artery. As a result, a range of values designed to mimic physiological oxygen concentrations supplied by the vasa vasorum to neglecting the presence of a vasa vasorum was used.

We show the oxygen contours of all 4 cases. We study the effect of oxygen transported by vasa vasorum by varying the oxygen partial pressure on the outer surface of the arterial wall. The physiological meaningful value of oxygen concentration 2.56×10^{-3} kg/m^3 represents a value of 50 mmHg. Thus, from 0 we increase each respective case two-fold to 6.4×10^{-4} kg/m^3 and 1.28×10^{-3} kg/m^3 until 2.56×10^{-3} kg/m^3 is reached. The baseline case is identified in red. We observe cases 1-3 as having the largest spatial distribution of hypoxic conditions seen thus far (**Figure 21**). Poor distribution of oxygen contours are observed. Only a slight change in contours is seen with the greatest distinction shown between cases 3 and 4. As a result, when the concentration of oxygen supplied by the vasa vasorum decreased to half its original value there are major effects. The wall is almost entirely depleted of essential oxygen. Furthermore, the

luminal range of oxygen diffusion is observed in case 1. High contours of oxygen concentration lie close to the *l-ilt* interface. Thus, the role of the vasa vasorum in supplying oxygen to the aorta is emphasized by these results.

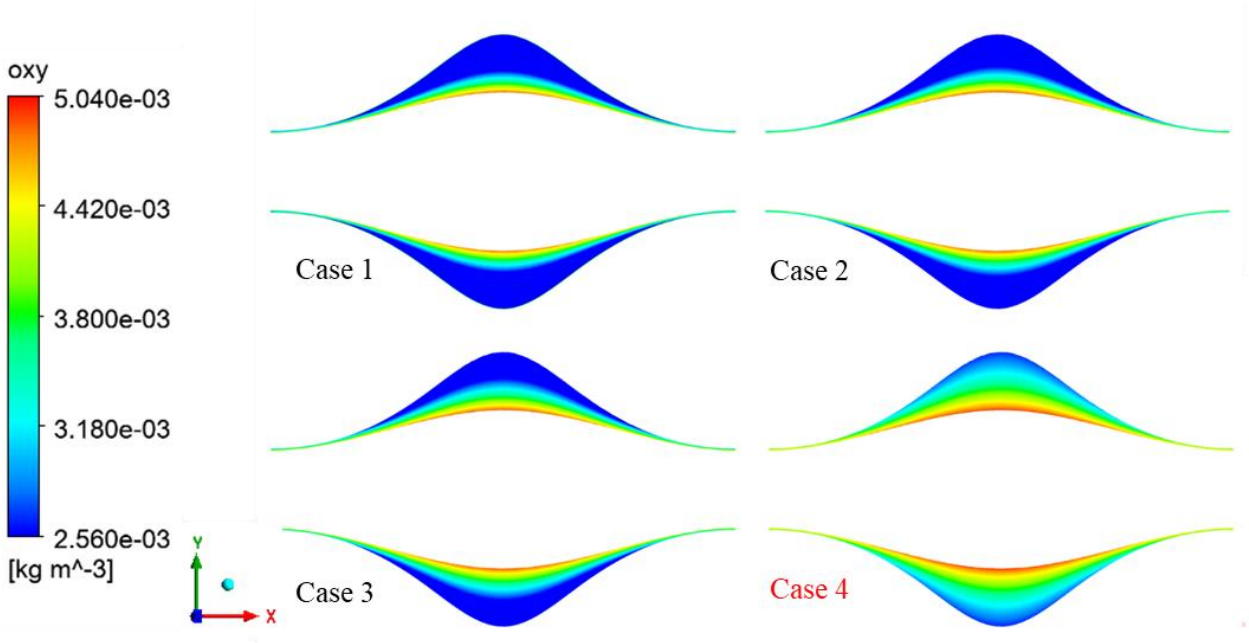

Figure 21 Oxygen contour plots of various vasa vasorum parameters. Analyzed oxygen concentrations varying external partial pressure oxygen to match physiological meaningful parameters. Cases 1-4 are 0 kg/m^3, 6.4 x 10^{-4} kg/m^3, 1.28 x 10^{-3} kg/m^3 and 2.56 x 10^{-3} kg/m^3 respectively.

To maintain a uniform protocol between parameters, the same lines were used to derive data points and are once again summarized in **Figure 22**. Cases 1-4 showed a pattern of decay with the steepest decrease in oxygen concentration found in case 1. The curve was dependent on the external partial pressure assigned in each case. This was also seen at the line drawn at the *ilt-w* interface. Each case showed a stepwise increase by two-fold at the apex of ILT thickness

relative to each assigned partial pressure. Moreover, case 4 shows a large difference in oxygen concentration between the proximal and distal neck of the ILT as compared to the apex. This shows the extent convection driven luminal oxygen transport was able to penetrate the ILT. In cases of hypoperfusion and vasa vasorum stenosis, the arterial wall is shown to suffer from oxygen deficiencies.

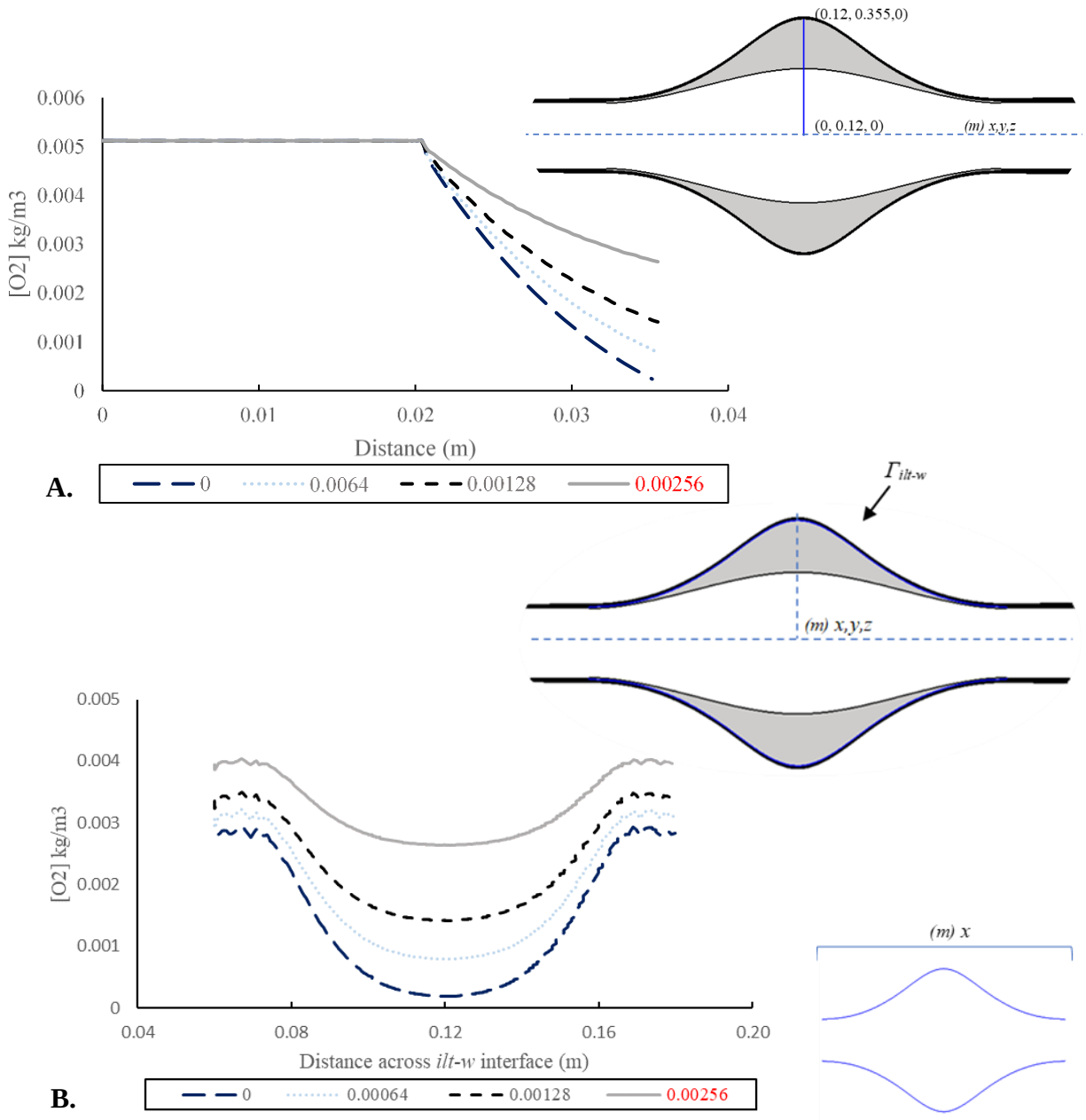

Figure 22 Quantitative plots of oxygen concentration for vasa vasorum. (A) Oxygen concentration along a vertical line in cases of varying external partial pressure. Top Right: Further defines location of derived data points. (B) Values taken from *ilt-w* interface in all cases. Bottom right: shows the outline and location of additional data points.

4.4 Effect of the Reaction Rate

We then study the effect of oxygen consumption by smooth muscle cells using an exponential trend in reaction rates that deviate from the baseline case. The pulsatile flow of blood within the artery creates a dynamic environment subject to hypertension and cardiac output. Oxygen consumption of vascular smooth muscle cells can increase with active vasoconstriction. Moreover, additional factors such as age, hormones and substrates can affect reaction rate. Thus, we use a range of values r = $8.4 \times 10^{-4}\ s^{-1}$, baseline of $8.4 \times 10^{-3}\ s^{-1}$,$8.4 \times 10^{-2}\ s^{-1}$,$8.4 \times 10^{-1}\ s^{-1}$.

Results of oxygen contours and quantitative plots are summarized. The spatial distribution of oxygen contours in cases 1-3 visually appear to be the same (**Figure 23**). The maximum value of oxygen concentration is shown at the *l-ilt* interface with a decline in the color-scale until hypoxic conditions are reached in the exterior. However, an increase in the reaction rate by two orders of magnitude compared to the baseline showed a greater hypoxic region. Thus, it is a reaction rate of $1.34 \times 10^{-11}\ s^{-1}$, well above the norm, that is shown to elicit any change in oxygen concentration within the ILT. In **Figure 24A** quantitative data is shown to support the visual contours of oxygen concentration. Case 4 is shown to decay more rapidly and results in a lower final oxygen concentration. In **Figure 24B**, a line across the *ilt-w* interface shows cases 1-3 bare the same results. Cases 1-3 show increased oxygen concentration at the apex of ILT thickness by a factor of 1.3 when compared to case 4. Convection driven oxygen transport is shown to penetrate *l-ilt* interface equally between cases. As a result, a change in the reaction rate affects exterior oxygen concentrations more readily. This is expected as luminal oxygen transport is constant while oxygen consumption increases in the arterial wall.

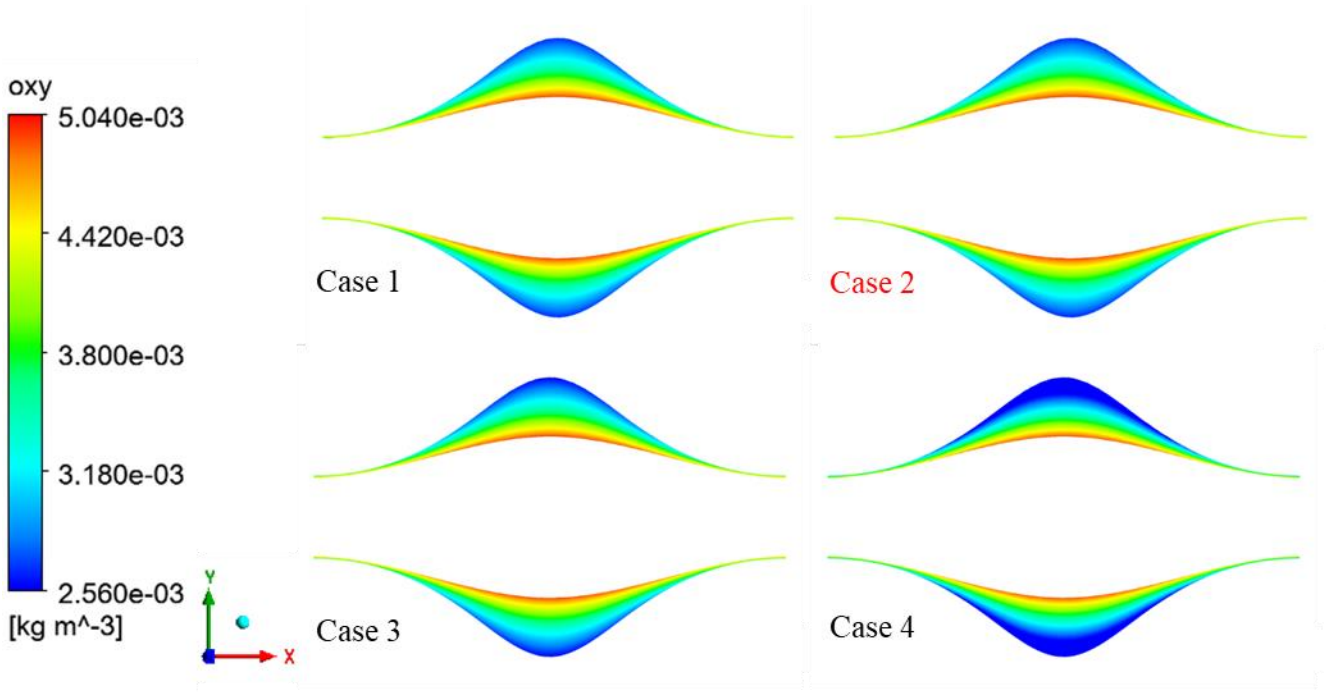

Figure 23 Oxygen contour plots of various reaction rate parameters. Analyzed oxygen concentrations varying reaction rates to match physiological meaningful parameters. Case 1-4 are of 8.4 x 10^{-4} s^{-1}, 8.4 x 10^{-3} s^{-1} , 8.4 x 10^{-2} s^{-1} and 8.4 x 10^{-1} s^{-1}.

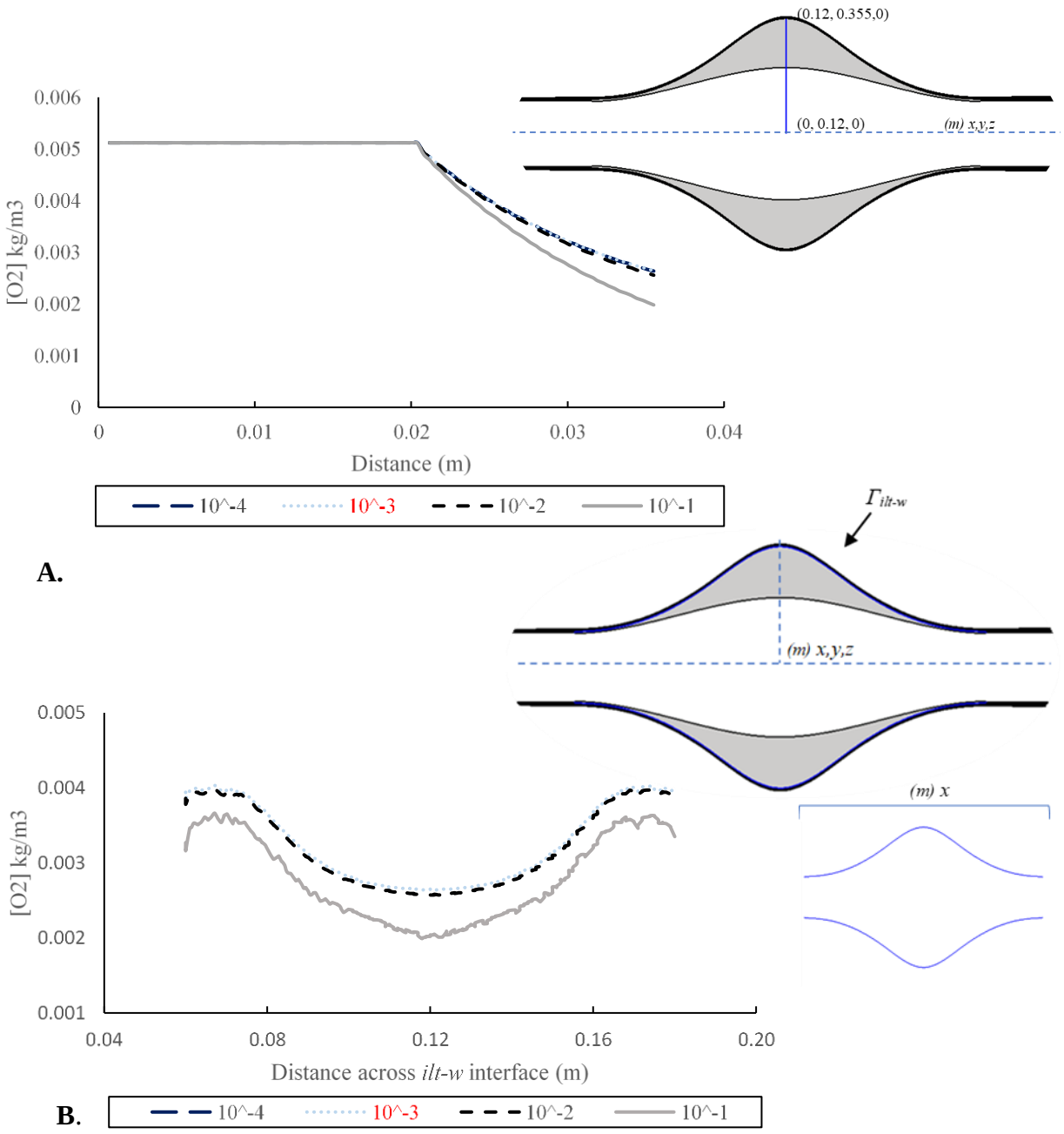

Figure 24 Quantitative plots of oxygen concentration for reaction rate (A) Oxygen concentration along a vertical line in cases of varying external partial pressure. Top Right: Further defines location of derived data points. (B) Values taken from *ilt-w* interface in all cases. Bottom right: shows the outline and location of additional data points.

4. 5 Effect of Flow Rate Input

For the final parameter, flow rate input is considered. Velocity at the inlet was previously defined by 0.235 m/s and subject to vessel diameter. Thus, we study the rate at which blood flow affects convection driven oxygen transport. Moreover, we study a range of values to encapsulate the dynamic environment of the cardiovascular system. Similar to the vasa vasorum, we decrease the baseline flowrate two-fold to 0.01175 m/s and 0.05875 m/s respectively. **Figures 11** and **12** show the results of the spatial oxygen distribution for the flow rate parameter. Both show no deviation from the baseline case. The same distribution of oxygen contours is seen and quantitative data follows the same trends.

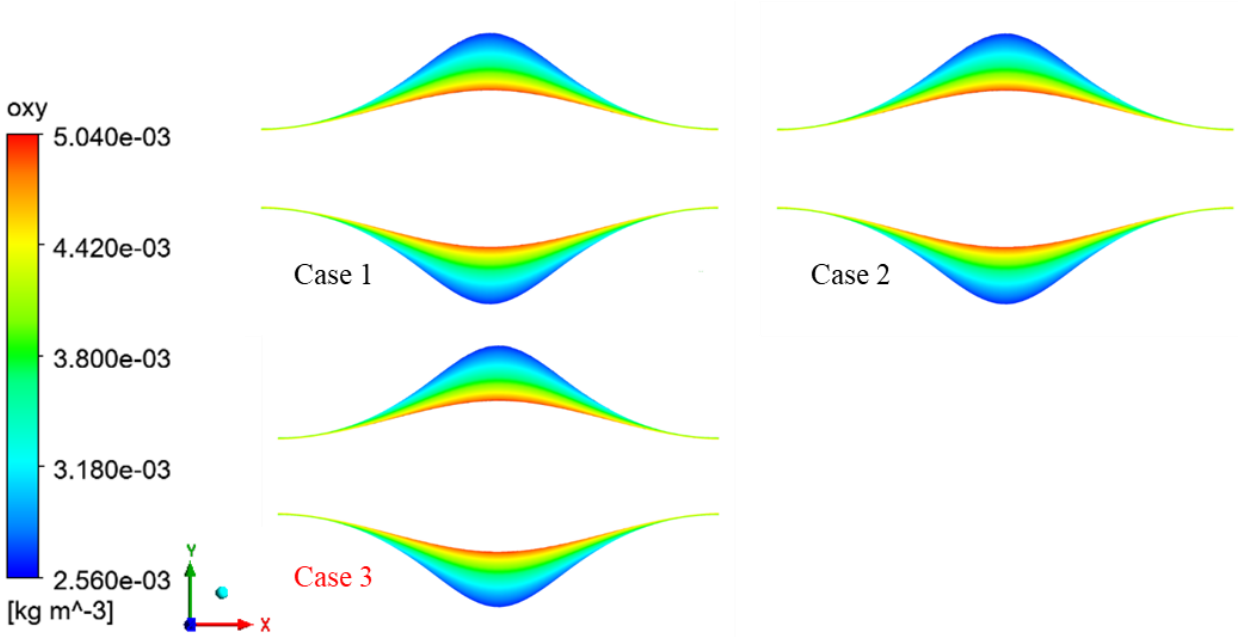

Figure 25 Oxygen contour plots of various flow rate parameters. Analyzed oxygen concentrations varying flow rate to match physiological meaningful parameters Cases 1-3 are 0.01175 m/s and 0.05875 m/s and 0.235 m/s respectively.

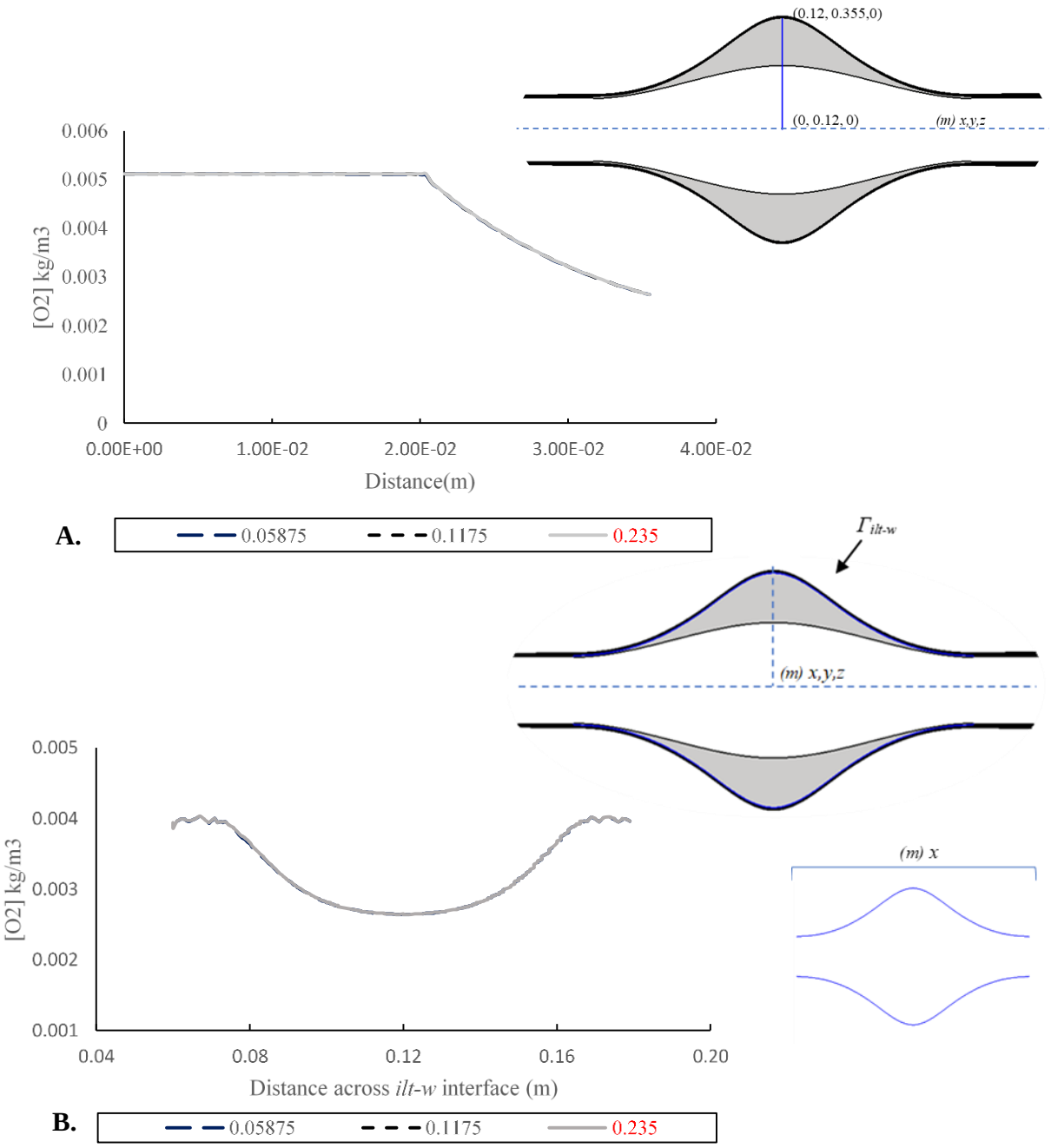

Figure 26 Quantitative plots of oxygen concentration for flowrate (A) Oxygen concentration along a vertical line in cases of varying external partial pressure. Top Right: Further defines location of derived data points. (B) Values taken from *ilt-w* interface in all cases. Bottom right: shows the outline and location of additional data points.

Chapter 5 – Discussion

We described a computational model of the abdominal aortic aneurysm encapsulating both hemodynamics and convection-diffusion driven oxygen transport. Discretized elements within the mesh were used to develop solution vectors providing oxygen contours, velocity streamlines and a total pressure profile. In this case, we used an idealized, 3D-axisymmetric model to perform a sensitivity analysis. This was done to investigate the effect of different physical parameters on oxygen transport. Moreover, analyze how mechanical features such as bulge diameter and ILT thickness affect spatial oxygen distribution throughout the vessel. We used physiological meaningful coefficients to adjust parameters such as oxygen diffusivity, external oxygen concentration supplied by the vasa vasorum, reaction rate and flowrate input. Some parameters like oxygen diffusivity and consumption cannot be directly measured. Thus, an exponential increase in values by one order of magnitude is oftentimes used to model conditions that deviate from the baseline model. Other parameters are reduced two-fold considering values that occur in a pathogenic vessel. Each case was relatively compared to the baseline model.

We discuss the results of all parameters. When varying bulge diameter and ILT thickness, ILT thickness was shown to have a large impact on oxygen concentration while bulge diameter had a minimal effect. This may negate the previous notion that the ILT serves as a mechanically protective layer in the aneurysm as thickness is closely associated with hypoxia. Moreover, our results support previous work done by Vorp using similar dimensions [5]. Additionally, previous studies have shown that the presence of an ILT results in poor diffusivity of the aneurysm and further reduces oxygen flux to the arterial wall [8]. Thus, characterizing properties of the ILT will be advantageous in risk of rupture analysis. In this case, ILT diffusivity was shown to have a minimal impact on oxygen concentration. The greatest decrease in oxygen concentration was

seen at a change in diffusivity by two orders of magnitude from baseline. On the other hand, wall diffusivity had a large impact with a uniform maximum oxygen concentration seen in the final case. Changes in arterial wall diffusivity can be associated with wall thickening or thinning and other vascular diseases. Atherosclerosis commonly occurs in conjunction with AAA leading to plaque formation and alteration of the elastin and collagen fibers of the arterial wall [30]. As a result, changes in wall diffusivity can lead to further weakening of the wall and an increased risk of rupture.

We then demonstrated a sensitivity analysis of a range of external oxygen concentrations representative of values neglecting the presence of a vasa vasorum, poorly vascularized AAAs and healthy vasculature. The AAA is subject to biomechanical remodeling showing increased stenosis and tissue ischemia [31]. This decreases perfusion by the vasa vasorum to the infrarenal aorta. Corresponding to previous computational models, a partial pressure of 50 mmHg was used in the baseline model as a normal oxygen concentration [15]. The vasa vasorum had one of the greatest effects on oxygen concentrations when compared to other parameters. Without the external, supplement of oxygen through these vessels, we observed that the interface between the ILT and the arterial wall is almost depleted of oxygen. Taking into account the physiological range of oxygen supplied by the VV can drastically improve oxygen transport in the ILT. Thus, oxygen concentration in the wall is sensitive to adventitial oxygen concentration suggesting that the vasa vasorum may play an important role in overall oxygen supply to the aortic wall.

We then discuss the reaction rate and flowrate input. The reaction rate was used to represent smooth muscle cell oxygen consumption. Results show a minimal effect on oxygen concentration. Thus, cardiovascular functions such as vasodilation and vasoconstriction may alter the metabolism of oxygen by smooth muscle cells but not enough to further degrade the

arterial wall. Moreover, flowrate input or the speed of blood flow showed no change in oxygen concentration. Thus, an increase in cardiac output within a specific time frame has no effect on oxygen delivery to the aneurysmal wall. Furthermore, compensatory mechanisms by the cardiovascular system may be ineffective at increasing oxygen delivery to the AAA.

In this study, the ILT is modeled as a rigid, solid domain. However, the ILT has semipermeable properties in the body. Thus, we will further address and quantify parameters through a porous model with a semipermeable ILT. Moreover, better simulate fluid-tissue interactions. Future directions include developing models that simulate pulsatile blood flow. This will increase our understanding on the effect of hemodynamics on oxygen localization within the AAA. Lastly, an extension of this work can include patient specific geometries. The axisymmetric geometry optimizes parameters allowing for more focused further studies. However, an AAA in practice is hardly symmetric and varies between patient to patient. Thus, changing arterial geometry will help obtain more realistic results.

References

1. Takayama T, Yamanouchi D. Aneurysmal Disease: The Abdominal Aorta. Surgical Clinics of North America. 2013;93(4):877-91. doi:https://doi.org/10.1016/j.suc.2013.05.005.
2. Patel MI, Hardman DT, Fisher CM, Appleberg M. Current views on the pathogenesis of abdominal aortic aneurysms. Journal of the American College of Surgeons. 1995;181(4):371-82.
3. Vorp DA. Biomechanics of abdominal aortic aneurysm. J Biomech. 2007;40(9):1887-902. doi:10.1016/j.jbiomech.2006.09.003.
4. Vorp DA, Mandarino WA, Webster MW, Gorcsan J, 3rd. Potential influence of intraluminal thrombus on abdominal aortic aneurysm as assessed by a new non-invasive method. Cardiovascular surgery (London, England). 1996;4(6):732-9. doi:10.1016/s0967-2109(96)00008-7.
5. Vorp DA, Wang DH, Webster MW, Federspiel WJ. Effect of intraluminal thrombus thickness and bulge diameter on the oxygen diffusion in abdominal aortic aneurysm. Journal of biomechanical engineering. 1998;120(5):579-83. doi:10.1115/1.2834747.
6. Virag L, Wilson J, Humphrey J, Karšaj I. A Computational Model of Biochemomechanical Effects of Intraluminal Thrombus on the Enlargement of Abdominal Aortic Aneurysms. Annals of biomedical engineering. 2015;43. doi:10.1007/s10439-015-1354-z.
7. Kemmerling EMC, Peattie RA. Abdominal Aortic Aneurysm Pathomechanics: Current Understanding and Future Directions. Advances in experimental medicine and biology. 2018;1097:157-79. doi:10.1007/978-3-319-96445-4_8.
8. Vorp DA, Lee PC, Wang DH, Makaroun MS, Nemoto EM, Ogawa S et al. Association of intraluminal thrombus in abdominal aortic aneurysm with local hypoxia and wall weakening. Journal of vascular surgery. 2001;34(2):291-9. doi:10.1067/mva.2001.114813.
9. Polzer S, Gasser TC, Markert B, Bursa J, Skacel P. Impact of poroelasticity of intraluminal thrombus on wall stress of abdominal aortic aneurysms. BioMedical Engineering OnLine. 2012;11(1):62. doi:10.1186/1475-925X-11-62.
10. Yan F, Jiang W-T, Xu Z, Wang Q-Y, Fan Y-B, Zhang M. Developing transmission line equations of oxygen transport for predicting oxygen distribution in the arterial system. Scientific reports. 2018;8(1):5369-. doi:10.1038/s41598-018-23743-2.
11. Annambhotla S, Bourgeois S, Wang X, Lin PH, Yao Q, Chen C. Recent advances in molecular mechanisms of abdominal aortic aneurysm formation. World J Surg. 2008;32(6):976-86. doi:10.1007/s00268-007-9456-x.
12. Wilson JS, Virag L, Di Achille P, Karsaj I, Humphrey JD. Biochemomechanics of intraluminal thrombus in abdominal aortic aneurysms. Journal of biomechanical engineering. 2013;135(2):021011-. doi:10.1115/1.4023437.
13. Ayyalasomayajula A, Vande Geest JP, Simon BR. Porohyperelastic finite element modeling of abdominal aortic aneurysms. Journal of biomechanical engineering. 2010;132(10):104502. doi:10.1115/1.4002370.
14. Raptis A, Xenos M, Dimas S, Giannoukas A, Labropoulos N, Bluestein D et al. Effect of macroscale formation of intraluminal thrombus on blood flow in abdominal aortic aneurysms. Computer methods in biomechanics and biomedical engineering. 2016;19(1):84-92. doi:10.1080/10255842.2014.989389.
15. Sun N, Leung JH, Wood NB, Hughes AD, Thom SA, Cheshire NJ et al. Computational analysis of oxygen transport in a patient-specific model of abdominal aortic aneurysm with

intraluminal thrombus. The British journal of radiology. 2009;82 Spec No 1:S18-23. doi:10.1259/bjr/89466318.
16. Adolph R, Vorp DA, Steed DL, Webster MW, Kameneva MV, Watkins SC. Cellular content and permeability of intraluminal thrombus in abdominal aortic aneurysm. Journal of vascular surgery. 1997;25(5):916-26. doi:10.1016/s0741-5214(97)70223-4.
17. Wang DH, Makaroun MS, Webster MW, Vorp DA. Effect of intraluminal thrombus on wall stress in patient-specific models of abdominal aortic aneurysm. Journal of vascular surgery. 2002;36(3):598-604. doi:10.1067/mva.2002.126087.
18. Tanaka H, Zaima N, Sasaki T, Hayasaka T, Goto-Inoue N, Onoue K et al. Adventitial vasa vasorum arteriosclerosis in abdominal aortic aneurysm. PloS one. 2013;8(2):e57398-e. doi:10.1371/journal.pone.0057398.
19. Billaud M, Hill JC, Richards TD, Gleason TG, Phillippi JA. Medial Hypoxia and Adventitial Vasa Vasorum Remodeling in Human Ascending Aortic Aneurysm. Front Cardiovasc Med. 2018;5:124-. doi:10.3389/fcvm.2018.00124.
20. Ritman EL, Lerman A. The dynamic vasa vasorum. Cardiovasc Res. 2007;75(4):649-58. doi:10.1016/j.cardiores.2007.06.020.
21. Tanaka H, Zaima N, Sasaki T, Sano M, Yamamoto N, Saito T et al. Hypoperfusion of the Adventitial Vasa Vasorum Develops an Abdominal Aortic Aneurysm. PLoS One. 2015;10(8):e0134386. doi:10.1371/journal.pone.0134386.
22. Iannetti L, D'Urso G, Conoscenti G, Cutrì E, Tuan RS, Raimondi MT et al. Distributed and Lumped Parameter Models for the Characterization of High Throughput Bioreactors. PLoS One. 2016;11(9):e0162774. doi:10.1371/journal.pone.0162774.
23. Caputo M, Chiastra C, Cianciolo C, Cutrì E, Dubini G, Gunn J et al. Simulation of oxygen transfer in stented arteries and correlation with in-stent restenosis. International journal for numerical methods in biomedical engineering. 2013;29(12):1373-87. doi:10.1002/cnm.2588.
24. Fraser KH, Meagher S, Blake JR, Easson WJ, Hoskins PR. Characterization of an abdominal aortic velocity waveform in patients with abdominal aortic aneurysm. Ultrasound in medicine & biology. 2008;34(1):73-80. doi:10.1016/j.ultrasmedbio.2007.06.015.
25. Buerk DG, Goldstick TK. Arterial wall oxygen consumption rate varies spatially. The American journal of physiology. 1982;243(6):H948-58. doi:10.1152/ajpheart.1982.243.6.H948.
26. Pittman. RN. Regulation of Tissue Oxygenation. Morgan & Claypool Life Sciences. 2011;
.
27. Popel AS. Theory of oxygen transport to tissue. Crit Rev Biomed Eng. 1989;17(3):257-321.
28. Xu J, Lu X, Shi G-P. Vasa vasorum in atherosclerosis and clinical significance. Int J Mol Sci. 2015;16(5):11574-608. doi:10.3390/ijms160511574.
29. Lucie Bacakova MT, Elena Filova, Roman Matějka, Jana Stepanovska, Jana Musilkova, Jana Zarubova, Martin Molitor. The Role of Vascular Smooth Muscle Cells in the Physiology and Pathophysiology of Blood Vessels. IntechOpen. 2018.
30. Tsamis A, Krawiec JT, Vorp DA. Elastin and collagen fibre microstructure of the human aorta in ageing and disease: a review. J R Soc Interface. 2013;10(83):20121004-. doi:10.1098/rsif.2012.1004.
31. Tanaka H, Zaima N, Sasaki T, Sano M, Yamamoto N, Saito T et al. Hypoperfusion of the Adventitial Vasa Vasorum Develops an Abdominal Aortic Aneurysm. PloS one. 2015;10(8):e0134386-e. doi:10.1371/journal.pone.0134386.